

# Euclid: Early Release Observations – The extended stellar component of the IC10 dwarf galaxy<sup>★</sup>

F. Annibali, A. M. N. Ferguson, P. M. Sanchez-Alarcon, P. Dimauro, L. K. Hunt, R. Pascale, M. Bellazzini, A. Lançon, et al.

(Full author list and affiliations details can be found after the references)

## ABSTRACT

We present a detailed analysis of the old, extended stellar component of the Local Group dwarf galaxy IC 10 using deep resolved-star photometry in the VIS and NISP bands of the *Euclid* Early Release Observations. Leveraging *Euclid*'s unique combination of wide field of view and high spatial resolution, we trace red giant branch (RGB) stars out to  $\sim 8$  kpc from the galaxy centre, reaching azimuthally-averaged surface brightness levels as faint as  $\mu_{H_E} \sim 29$  mag arcsec $^{-2}$ . Our analysis reveals that IC 10's stellar distribution is significantly more extended than previously thought. After correcting for foreground extinction and subtracting contamination from Milky Way stars and background galaxies, we derive a radial stellar density profile from RGB star counts. The profile shows a marked flattening beyond  $\sim 5$  kpc, and is best fit by a two-component (Sérsic + exponential) model, yielding a total stellar mass in old (age  $\gtrsim 1$  Gyr) stars of  $M_\star = (6.7\text{--}8.1) \times 10^8 M_\odot$ . The origin of the outer stellar component is unclear. It may be accreted, even possibly associated with the counter-rotating H $\text{\scriptsize I}$  gas in the outer regions of IC 10, or it may represent an ancient 'in-situ' stellar halo. We tentatively detect two symmetric stellar overdensities at the edge of our imagery. These roughly align with the direction of IC 10's orbit around M31, suggesting that they may be signatures of tidal stripping. As part of our analysis, we derive a new distance to IC 10 based on the RGB tip, finding  $D = 762 \pm 20$  kpc and the distance modulus is  $(m - M)_0 = 24.41 \pm 0.05$ .

**Key words.** Galaxy: evolution – Galaxy: structure – techniques: photometric – Stars: imaging

## 1. Introduction

In the  $\Lambda$  cold dark matter ( $\Lambda$ CDM) cosmological framework (Peebles 1982), structure formation proceeds hierarchically through the successive merging and accretion of smaller dark-matter haloes (White & Rees 1978; Springel et al. 2006), a process that begins at early cosmic times and continues down to the present day (Fakhouri et al. 2010; De Lucia & Helmi 2008). As a result, galaxies today are expected to be embedded in extended stellar haloes formed from the disrupted remnants of accreted satellites, and to be surrounded and orbited by numerous smaller companions and stellar streams (Bekki & Chiba 2001; Bullock & Johnston 2005; Johnston et al. 2008; Cooper et al. 2010).

This picture has been extensively confirmed for massive galaxies, both spirals and ellipticals, which show abundant observational evidence of past accretion events (e.g., Ibata et al. 2001b,a; Ferguson et al. 2002; Belokurov et al. 2006; Martínez-Delgado et al. 2010; Crnojević et al. 2016). Dwarf galaxies, traditionally seen as the fundamental building blocks of larger systems, are likewise expected to grow via the accretion of even smaller structures (Diemand et al. 2008; Wheeler et al. 2015). However, direct evidence for accretion events around dwarfs remains much more elusive than for massive galaxies (Martínez-Delgado et al. 2008; Koposov et al. 2018; Paudel et al. 2018; Carlin et al. 2019; Kado-Fong et al. 2020; Correnti et al. 2025). It is still unclear whether dwarf galaxies host stellar haloes at all (Chiti et al. 2021; Tarumi et al. 2021; Deason et al. 2022; Kado-Fong et al. 2022). While  $\Lambda$ CDM simulations predict similar relative amounts of substructure across halo mass scales (Diemand et al. 2008), the amount

of stellar mass these systems can accrete over time is poorly constrained (Kang & Ricotti 2019; Martin et al. 2021; Deason et al. 2022; Cooper et al. 2025). This uncertainty largely stems from the poorly known stellar mass–halo mass (SMHM) relation and the low halo occupation fraction at the smallest masses (Sales et al. 2022, and references therein). As a matter of fact, all simulations consistently indicate that the stellar haloes of individual dwarf galaxies, if present, are expected to be extremely faint and challenging to detect, whereas cold tidal features, such as streams and shells, tend to stand out above the average surface brightness profile, making them comparatively easier to observe (Annibali et al. 2016; Belokurov & Koposov 2016; Román et al. 2023; Sacchi et al. 2024). An additional challenge in detecting stellar haloes around dwarf galaxies is that much of the accreted, ex-situ stellar mass is expected to project onto the central regions of the galaxy, where it is blended with the typically dominant in-situ stellar population (e.g., Pillepich et al. 2015; Cooper et al. 2025). This overlap complicates efforts to disentangle the two components observationally. As a result, robust identification of the accreted stellar halo requires tracing the stellar distribution to large galactocentric radii and reaching extremely low surface brightness levels (Chiti et al. 2021; Sestito et al. 2023; Jensen et al. 2024).

In this paper, we search for and study the extended stellar component around the Local Group dwarf galaxy IC 10 ( $M_V \sim -15$ , McConnachie 2012). Argued to be the closest example of a starburst galaxy (Richer et al. 2001), IC 10 is a fascinating object whose stellar component has been poorly studied due to its low Galactic latitude ( $b \sim -3^\circ 3$ ). This sightline leads to significant foreground contamination from the stars and dust of the Milky Way (MW), with the result being that many of IC 10's properties are still rather uncertain. In particu-

<sup>★</sup> This paper is published on behalf of the Euclid Consortium.

lar, estimates of its current star-formation rate range from 0.04–0.5  $M_{\odot}$  yr $^{-1}$  (Koch et al. 2025; Binder et al. 2025), and distance estimates range from  $\sim 500$  kpc to  $\sim 1$  Mpc (e.g. Jacobs et al. 2009; Sanna et al. 2008; Hunter 2001; Gholami et al. 2025). Also, its stellar mass is highly uncertain, with quoted values ranging from  $\sim 0.9 \times 10^8 M_{\odot}$  to  $\sim 4 \times 10^8 M_{\odot}$ , a spread that cannot be attributed solely to distance uncertainties (Lee et al. 2003; McConnachie 2012; Pace 2024; Nersesian et al. 2019).

As a distant satellite of M31, IC 10 may have experienced one or more interactions with other systems. Several studies have shown that IC 10 hosts an extended and disturbed H $\alpha$  disc, including counter-rotating gas in its outskirts (Shostak & Skillman 1989; Wilcots & Miller 1998; Namumba et al. 2019). Nidever et al. (2013) also identified a long north-west H $\alpha$  feature with a strong velocity gradient, later confirmed by Namumba et al. (2019). Using the proper motions from Brunthaler et al. (2007), they argued that this structure is unlikely to result from tidal forces or ram-pressure stripping due to M31, and instead may reflect an interaction or merger with another dwarf. Deep imaging has not revealed clear stellar tidal features (Demers et al. 2004; Sanna et al. 2010), and an apparent offset between young and old populations (Gerbrandt et al. 2015) was not confirmed by Howell et al. (2025). Orbital modelling by Bennet et al. (2024) suggests a  $\sim 130$  kpc pericentre passage around M31 about 1–2 Gyr ago. Altogether, these findings point to a past interaction, making the structure of IC 10’s extended stellar component a valuable piece of information of its evolutionary history.

In Sect. 2 of this paper we describe the data reduction and the photometric analysis, while in Sect. 3 we present the final cleaned, reddening-corrected colour-magnitude diagrams (CMDs) and derive the galaxy distance from the tip of the red giant branch (RGB). Sect. 4 describes the spatial distribution of IC 10’s stellar population and the inferred radial profile. We discuss our results in a larger context in Sect. 5, and give our summary in Sect. 6.

## 2. Data reduction and photometry

IC 10 was observed in 2023 during the *Euclid* performance verification (PV) phase as part of the Showcase Galaxies Early Release Observation (ERO) program (Cuillandre et al. 2025; Hunt et al. 2025, hereafter C25; H25). While the other Showcase galaxies were acquired with one standard Reference Observation Sequence (ROS), consisting of 4 dithered exposures, of 560 s for VIS (Euclid Collaboration: Cropper et al. 2025) and 87 s for each NISP (Euclid Collaboration: Jahnke et al. 2025) band<sup>1</sup> ( $I_{\text{E}}$ ,  $J_{\text{E}}$ , and  $H_{\text{E}}$ ), typical of the Euclid Wide Survey (EWS, Euclid Collaboration: Scaramella et al. 2022), IC 10 was observed for a longer exposure time consisting of 2 ROS, totalling about 2 hours with overheads.

As with the other ERO galaxies, IC 10 was not reduced with the standard Science Ground Segment pipeline (Euclid Collaboration: Romelli et al. 2025), but rather with a procedure optimised for the study of the low surface brightness (LSB) emission, developed by C25. In brief, this pipeline processes the calibrated level 1 raw VIS and NISP images removing cosmic rays, correcting for geometric distortions, masking persistence effects due to preceding spectroscopic observations, and

applying a ‘super flat field’ that includes the illumination pattern and low-level flux non-linearity.

The final stacked frames have a median point spread function (PSF) full width at half maximum (FWHM) of 0''.16, 0''.47, 0''.47, and 0''.49 (1.57, 1.57, 1.58, 1.65 pixels) in  $I_{\text{E}}$ ,  $J_{\text{E}}$ ,  $J_{\text{E}}$ , and  $H_{\text{E}}$ , respectively. For both instruments, the PSF is slightly undersampled, given the pixel sizes of 0''.1 and 0''.3 of the VIS and NISP images, respectively. The ERO data were rescaled to have a nominal zero point of ZP=30.13 AB mag for  $I_{\text{E}}$  and ZP=30.0 AB mag for  $J_{\text{E}}$ , and  $H_{\text{E}}$  (C25; H25). Figure 1 shows a colour-combined image of the galaxy ( $I_{\text{E}}$ =blue,  $J_{\text{E}}$ =green, and  $H_{\text{E}}$ =red) with the stretch optimized to highlight the morphology of the old stellar component.

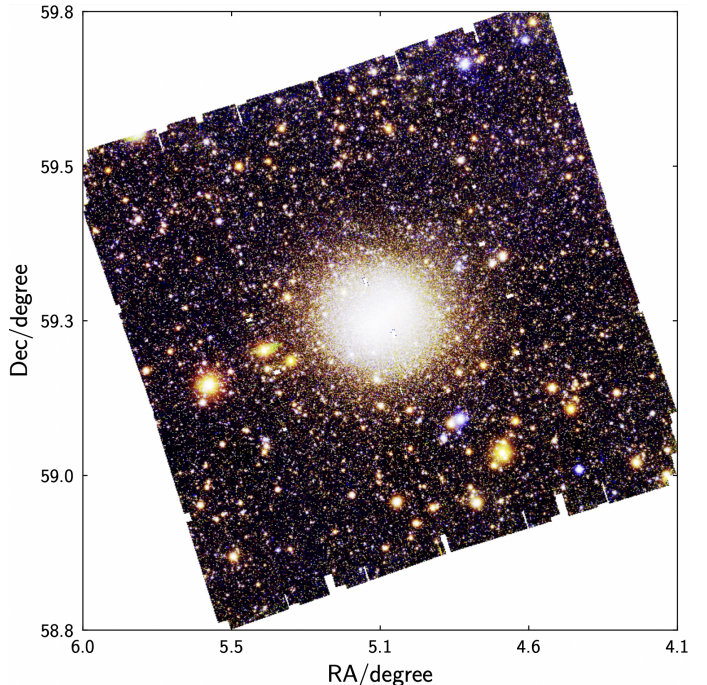


**Fig. 1.** *Euclid* colour-combined ( $I_{\text{E}}$  in blue,  $J_{\text{E}}$  in green, and  $H_{\text{E}}$  in red) image of IC 10 with the stretch optimized to highlight the morphology of the old stellar component. North is up and east is left.

### 2.1. Point source photometry

Photometry was performed with the DAOPHOT package (Stetson 1987) in the IRAF environment.<sup>2</sup> Given our focus on the extended low stellar density component of IC 10, aperture photometry is well suited to our goals, offering performance comparable to PSF-fitting methods in this regime.

We detected sources by running the DAOFIND routine independently in each of the four *Euclid* photometric bands, adopting a threshold of 3 times the average background standard deviation  $\sigma_{\text{bg}}$  derived from several 20 pixel $\times$ 20 pixel external regions devoid of stars. For each band, aperture photometry was performed at the position of the detected sources with the PHOT task adopting an aperture of 1.5 pixels in radius, corresponding to 0''.15 and 0''.45 in VIS and NISP, respectively (i.e., corresponding roughly to the PSF FWHM). The local background was computed within an annulus of 15–20 pixel radius centred on each source. For

<sup>1</sup> The quoted values correspond to the effective exposure times, while the total durations reported in Euclid Collaboration: Scaramella et al. (2022) also account for observational overheads.

<sup>2</sup> IRAF is distributed by the National Optical Astronomy Observatory, which is operated by the Association of Universities for Research in Astronomy, Inc., under cooperative agreement with the National Science Foundation.

VIS, we also computed photometry in a larger aperture of 2 pixel radius to allow for removal of saturated stars and extended sources, as detailed below. Aperture corrections from 1.5 pixel radius to larger apertures of 3'' for VIS and 9'' for the NISP images, totalling about 20 times the PSFs' FWHM and capturing  $\gtrsim 98\%$  of the total PSF flux (C25), were computed selecting the brightest unsaturated, most isolated stars, and subtracting nearby neighbours through a PSF model derived for each band with the DAOPHOT PSF task (see Appendix C for more details on the PSF model assumptions). The derived aperture corrections are  $-0.56 \pm 0.02$ ,  $-0.32 \pm 0.05$ ,  $-0.34 \pm 0.05$ , and  $-0.46 \pm 0.05$  mag in  $I_E$ ,  $Y_E$ ,  $J_E$  and  $H_E$ , respectively. Finally, the magnitudes were calibrated applying the zero points of C25.

The four photometric catalogues in  $I_E$ ,  $Y_E$ ,  $J_E$ , and  $H_E$  were cross-matched adopting a 0''.5 maximum tolerance in position (about the size of the NISP PSF FWHM), resulting in 418 484 sources that have photometry in all bands. The cross-match removes the majority of spurious detections, like cosmic rays, peaks on bright star spikes, or residual artifacts from the image reduction pipeline. We then applied selection cuts based on the DAOPHOT photometric errors in all four bands, retaining only sources within 3 times the standard deviation of the error distribution as a function of magnitude.

Bright, saturated stars and extended objects were then removed based on diagnostics that quantify the deviation from a stellar profile. More specifically, we identified objects that deviate from the PSF based on their ‘concentration index’, namely by comparing aperture photometry at two different apertures (see, e.g., Peng et al. 2011). Our approach is illustrated in Fig. 2, where we show the VIS photometry computed within a 1.5 pixel radius aperture,  $I_E(1.5 \text{ pix})$ , versus  $\Delta I_E = I_E(1.5 \text{ pix}) - I_E(2 \text{ pix})$ , that is to say the difference in magnitude between photometry at 1.5 and 2 pixels, respectively. Relatively bright unsaturated stars populate a narrow region around  $\Delta I_E \sim 0.18$ . On the other hand, bright saturated stars with  $I_E(1.5 \text{ pix}) \leq 19.5$  tend to have larger  $\Delta I_E$  values, due to the loss of flux in the most central pixels. At fainter magnitudes, large positive  $\Delta I_E$  values are typically due to extended background galaxies, with flatter profiles than the PSF, while negative values are associated with spurious detections and residual bad pixels. We selected sources within 2 times the standard deviation from the mode of the distribution and conservatively discarded all sources brighter than  $I_E(1.5 \text{ pix}) = 19.5$ , independently of their  $\Delta I_E$  value, as potentially saturated (see Fig. 2). In the end, we are left with 336 957 sources. However, these selections remove only the most obvious contaminants, while compact background galaxies, as well as compact stellar clusters, are retained in the photometric catalogue.

## 2.2. Reddening correction

The reddening correction was performed in two steps, considering both far-infrared (FIR) dust maps and the *Euclid* colours of resolved stars.

Initially, we applied a spatially variable extinction correction to all sources based on the Schlegel et al. (1998) reddening maps, as described in H25. Specifically, the foreground extinction at each source’s position was estimated through the publicly available Python package `dustmaps`,<sup>3</sup> assuming the recalibration of Schlafly & Finkbeiner (2011). At each location, the code returns the corresponding  $E(B - V)$  value derived through linear

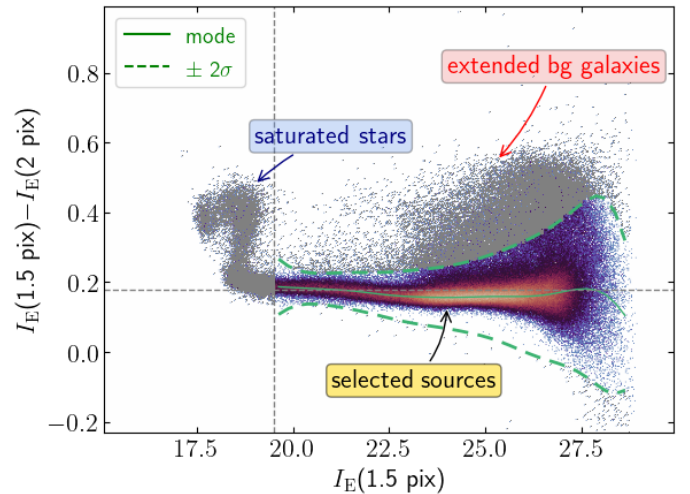


**Fig. 2.** Our source selection based on the distribution in the  $I_E(1.5 \text{ pix}) - I_E(2 \text{ pix})$  versus  $I_E(1.5 \text{ pix})$  plane. Point sources populate a narrow region around  $\Delta I_E \sim 0.18$ , while bright saturated stars and extended background galaxies tend to have larger values. We retained all sources within  $2\sigma$  of the mode of the distribution, as indicated by the dashed green line, and furthermore discarded bright stars with  $I_E(1.5 \text{ pix}) \leq 19.5$ .

interpolation on the dust maps. Figure 3 (top) shows the  $E(B - V)$  map derived across the full *Euclid* FoV. The field exhibits strong and spatially variable reddening, with  $E(B - V)$  increasing from  $\sim 0.6$  mag to  $\sim 1$  mag from south-east to north-west. The highest values near the galaxy centre [ $E(B - V) \sim 1.4$ ] are spurious, caused by IC 10 contamination not properly removed from the Schlegel et al. (1998) dust maps. We therefore masked a central 8' radius region and assigned it a constant reddening of  $E(B - V) = 0.78$ , corresponding to the  $3\sigma$ -clipped mean  $E(B - V)$  in an adjacent  $\sim 0.6$ -wide annulus. The resulting masked map (Fig. 3, bottom) was used to apply a first-order extinction correction to individual sources in our photometric catalogue. The  $E(B - V)$  values were converted into  $A_V$  adopting  $R_V = 3.1$ . Extinction values in the *Euclid* bands were derived adopting the photometric bands from Laureijs et al. (2011), the extinction curve from Gordon et al. (2023),<sup>4</sup> and assuming a G2V stellar spectrum, taken as a compromise between the blue and the red populations studied in this work. This provides relative ratios of  $A_\lambda/A_V = 0.726, 0.375, 0.266$ , and  $0.173$ , for  $I_E$ ,  $Y_E$ ,  $J_E$ , and  $H_E$ , respectively.

Since this initial correction only accounts for foreground extinction and the Schlegel et al. maps lack the resolution to capture small-scale variations, we implemented a second, more refined procedure based on the colour of RGB stars. Before this second step, foreground contaminants were removed from the catalogue by applying cuts in a colour-colour diagram as described in Sect. 2.3 and Appendix A, using foreground reddening-corrected magnitudes to achieve a cleaner separation between IC 10 and Galactic stars.

The cleaned  $H_E$  versus  $I_E - H_E$  CMD in Fig. 4a, with magnitudes not corrected for extinction, shows a significant colour spread of  $\Delta(I_E - H_E) \sim 1.4$ . Although age and metallicity play a role, differential reddening is the main cause. In fact, the  $E(B - V)$  variations shown in Fig. 3 translate into variations in  $E(I_E - H_E)$  of  $\sim 1$  mag or more, which exceed, for

<sup>3</sup> `dustmaps` is found at <https://dustmaps.readthedocs.io/en/latest/maps.html> and the dust maps themselves can be accessed and downloaded in the context of this package.

<sup>4</sup> The G23 extinction curve also incorporates results by Gordon et al. (2009), Fitzpatrick et al. (2019), Gordon et al. (2021), and Decleir et al. (2022).

instance, the  $\sim 0.5$  mag shift in colour at the RGB tip predicted by stellar models (Bressan et al. 2012; Marigo et al. 2017) when assuming a spread in metallicity from  $[M/H] = -1.4$  to the present-day value of about  $-0.4$  derived in H II regions by Magrini & Gonçalves (2009).

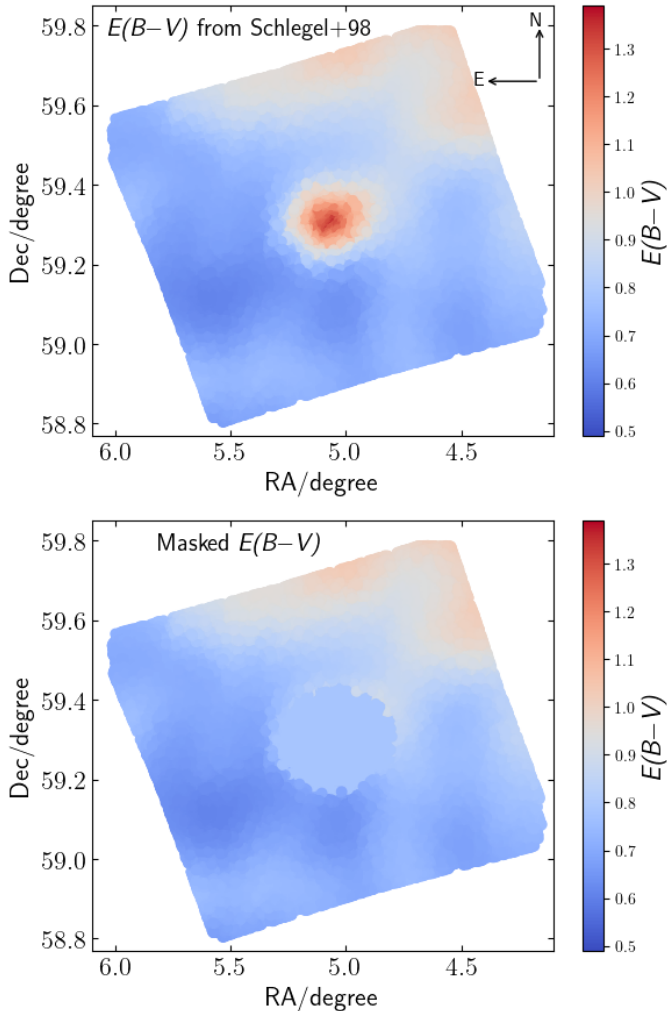


**Fig. 3.** *Top:* spatial map of  $E(B - V)$  in IC 10 over the entire *Euclid* FoV as derived from the *dustmaps* code assuming the Schlegel et al. (1998) dust maps. Foreground extinction increases from south-east to north-west. The high  $E(B - V)$  values at the centre of the field are due to spurious contamination from IC 10 in the dust maps. *Bottom:*  $E(B - V)$  masked spatial map, where we have assigned to a central  $8'$ -radius circular region a constant reddening value equal to the average  $E(B - V)$  computed in an adjacent external annulus.

We selected RGB stars within the polygon outlined in Fig. 4a and inferred a ‘reference’ RGB line (yellow curve) from a sub-sample in a relatively low extinction region, with a median value from the Schlegel’s maps of  $E(B - V) \sim 0.65$  (dashed ellipse in Fig. 4b). The reference RGB line presents some wiggles, likely due to residual foreground MW stars not removed by our selections. Starting from the reference RGB line, we generated a grid of RGB lines for extinctions in the range of  $0 < E(B - V) < 1.6$ , in steps of  $\Delta E(B - V) = 0.01$ , adopting the  $A_\lambda/A_V$  values reported before in this section.

Ultimately, our extinction map was derived following an approach similar to that described in Sarajedini et al. (2007) and Milone et al. (2012). For each RGB star selected within the polygon in Fig. 4a, we identified the 50 nearest RGB neighbours in

the image, from which we computed a median  $H_E$  magnitude and  $I_E - H_E$  colour. Then, the best-fit RGB line reproducing these median values provided the  $E(B - V)$  value at the location of each star. This allows us to construct a spatial map of extinction.

This method relies on the assumption that the RGB population is uniform across the entire field of view, so that any displacement from the reference sequence can be attributed solely to reddening variations. This inevitably prevents us from probing possible age or metallicity gradients within the RGB population, but given the severe and highly inhomogeneous foreground extinction toward IC 10, this assumption is unavoidable.

Our results are displayed in Fig. 4b. At the very centre of IC 10, the hole in the extinction map is due to severe stellar crowding, which prevents us from resolving individual RGB stars. The poorer sampling in the outermost regions is caused by the decrease in star counts with increasing distance from the IC 10 centre. The derived reddening values (internal plus foreground) are in the range  $0.4 \lesssim E(B - V) \lesssim 1.4$ , which is compatible with the range covered by the Schlegel et al. map. However, the spatial resolution of the  $E(B - V)$  map derived from resolved star counts is remarkably better than the latter, revealing the presence of filaments, knots, and spatial variations on scales of  $\sim 1'$ . An approach based on resolved stars was also used by Sanna et al. (2008) for a small region of IC 10 observed with the *Hubble* Space Telescope. Although a large fraction of their footprint falls in the central hole in our map, there is still some overlap between the two sets of photometry; for the region in common, our map provides a median reddening of  $E(B - V) = 0.8 \pm 0.1$ , in excellent agreement with their value of  $E(B - V) = 0.78 \pm 0.06$  inferred from deep CMD analysis.

Lastly, in Fig. 4c we compare our results with the FIR dust emission map from *Herschel* SPIRE/250 taken from the Dwarf Galaxy Survey (Madden et al. 2013). The agreement between the two is remarkable, with high extinction regions in our map corresponding to peaks in the *Herschel* emission map and, vice-versa, low  $E(B - V)$  values being associated with depression values in the FIR emission. The excellent agreement between the two maps showcases the power of the resolved-star approach for deriving high-resolution reddening maps toward nearby galaxies affected by high extinction. In the end, we used the extinction map of Fig. 4b, to correct the entire (including also foreground stars) photometric catalogue.

### 2.3. Foreground star contamination

IC 10 suffers major contamination from Galactic foreground stars, mainly from the MW disc. In order to remove as many of these contaminating sources as possible, we followed the same procedure as in H25, based both on *Gaia* proper motions and parallaxes, and on selection of sources in a colour-colour diagram. We describe the procedure in details in Appendix A. After removal of contaminants, the final IC 10 photometric catalogue with reliable sources having photometry in all four *Euclid* bands contains 227 128 stars.

## 3. Colour-magnitude diagrams

The final calibrated, reddening corrected,  $H_{E,0}$  versus  $I_{E,0} - H_{E,0}$  and  $J_{E,0}$  versus  $Y_{E,0} - H_{E,0}$  CMDs of resolved stars in IC 10 are shown in Fig. 5. We show also the  $I_{E,0}$  versus  $I_{E,0} - Y_{E,0}$  and  $I_{E,0}$  versus  $I_{E,0} - H_{E,0}$  CMDs in Fig. B.1 in Appendix B.

The CMD in Fig. 5a is before removal of the contaminants described in Sect. 2.3. Stars in IC 10, mainly RGB and AGB

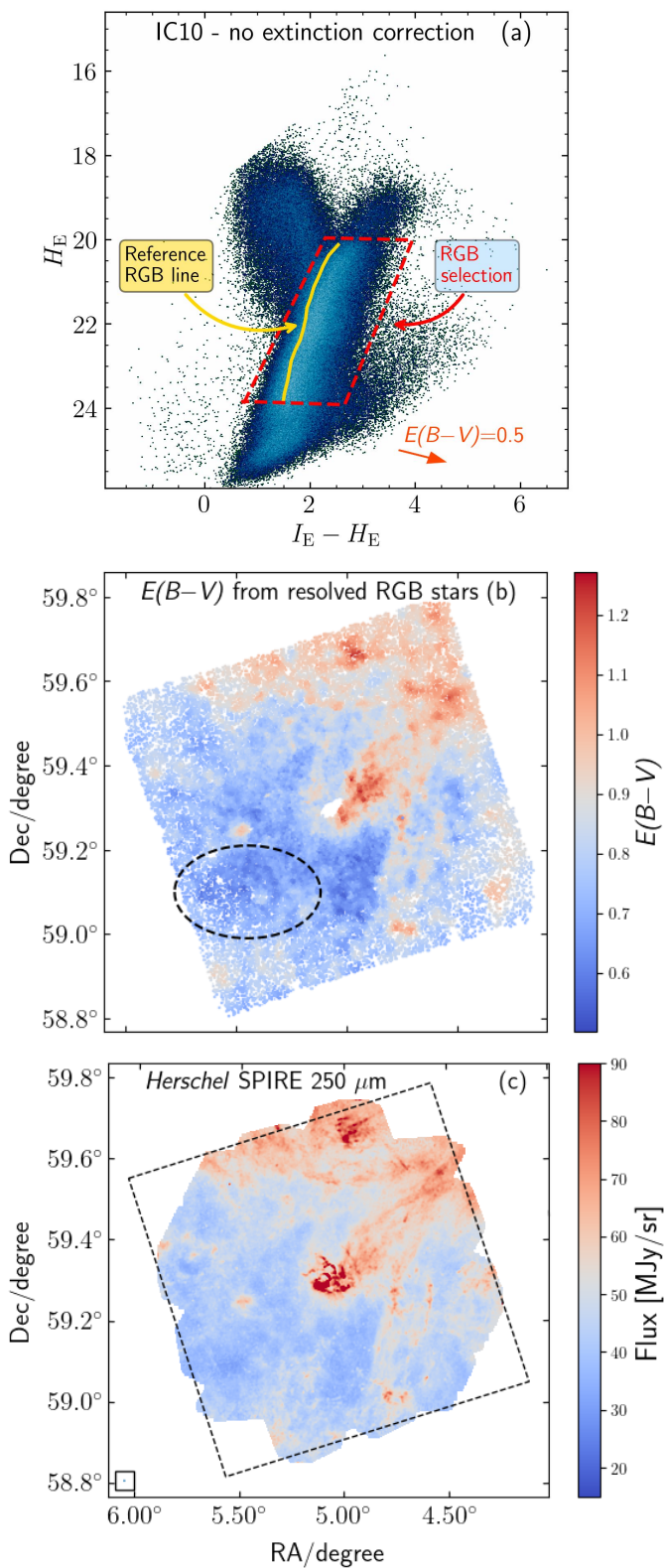


**Fig. 4.** Panel (a):  $H_E$  versus  $I_E - H_E$  CMD of IC 10 before reddening correction. The red polygon indicates our selection of RGB stars for the dust distribution, while the yellow curve is the reference RGB line with  $E(B - V) \sim 0.65$ . The orange arrow is the reddening vector for  $E(B - V) = 0.5$ . Panel (b):  $E(B - V)$  map derived from the RGB resolved stars, as described in Sect. 2.2. The dashed ellipse denotes the region used to infer the reference RGB line displayed in (a). Panel (c): FIR dust emission map from *Herschel* SPIRE/250 taken from Madden et al. (2013). The *Euclid* footprint is indicated for reference as a dotted square.

stars, define a distinct sequence that extends from  $I_{E,0} - H_{E,0} \sim 3$ ,  $H_{E,0} \sim 18$  down to  $I_{E,0} - H_{E,0} \sim -1$ ,  $H_{E,0} \sim 25.5$ ; on the other hand, Galactic disc stars appear organized along a different sequence that runs from  $I_{E,0} - H_{E,0} \sim -1$ ,  $H_{E,0} \sim 17$  to  $I_{E,0} - H_{E,0} \sim 2$ ,  $H_{E,0} \sim 24$ , and give the semblance of an X-feature on the CMD. Bright foreground contaminants identified through *Gaia* proper motions and parallaxes (see Sect. 2.3), over-plotted on the total CMD, amount to just a minor fraction of the total contamination from blue MW stars.

The final cleaned CMD that is displayed in Fig. 5b still suffers from major contamination by MW foreground stars that are bluer than  $I_{E,0} - H_{E,0} \sim 1$  and brighter than  $H_{E,0} \sim 21$ , while redder and fainter Galactic M dwarf stars appear to have been largely successfully removed. In the clean diagram, the cloud of blue stars at  $I_{E,0} - H_{E,0} \lesssim -1$ ,  $H_{E,0} \gtrsim 22$ , is compatible both with blue BP stars in IC 10, i.e. massive main sequence (MS) stars and post-MS stars in the hot core helium-burning phase, with ages  $\lesssim 200$  Myr (see also Fig. 5c for a direct comparison with stellar models) and with Galactic WDs. However, as already discussed in Sect. 2.3, these sources appear distributed quite homogeneously over the *Euclid* FoV, indicating the vast majority of them are Galactic WDs rather than BP stars in IC 10.

In the CMD, we further identify a vertical sequence of red supergiants (RSG) at  $I_{E,0} - H_{E,0} \sim 1.5$ ,  $15.5 \lesssim H_{E,0} \lesssim 18$ , with ages from  $\sim 20$  Myr to  $\sim 50$  Myr; luminous (as bright as  $H_{E,0} \sim 18$ ) and red ( $1 \lesssim I_{E,0} - H_{E,0} \lesssim 5$ ) AGB stars with ages from  $\sim 0.1$  Gyr to a few Gyrs; RGB stars with  $0 \lesssim I_{E,0} - H_{E,0} \lesssim 2$ ,  $H_{E,0} \gtrsim 19.7$  and ages older than 1–2 Gyr (and potentially as old as  $\sim 13$  Gyr). Also visible at  $-1 \lesssim I_{E,0} - H_{E,0} \lesssim 1$ ,  $H_{E,0} \gtrsim 24$ , toward our detection limit, is a hint of the red clump (RC), populated by low-mass stars in the core-helium burning phase, with ages  $> 1$ –2 Gyr. Faint red sources at  $I_{E,0} - H_{E,0} \gtrsim 2.5$ ,  $H_{E,0} \gtrsim 21$  are residual background galaxies, based both on direct visual inspection on the images and on their uniform spatial distribution.

In Fig. 5c, the  $H_{E,0}$  versus  $I_{E,0} - H_{E,0}$  CMD is compared with the PARSEC stellar isochrones (Bressan et al. 2012; Chen et al. 2014, 2015; Tang et al. 2014; Marigo et al. 2017; Pastorelli et al. 2019, 2020) in the *Euclid* bands, shifted according to a distance modulus of  $(m - M)_0 = 24.41$ , which corresponds to a distance of  $D = 0.762$  Mpc derived in Sect. 3.1. We display isochrones for stellar ages in the range of 10 Myr–10 Gyr. Metallicities as low as  $Z = 0.004$  and  $Z = 0.001$  ( $\sim 26\%$  and  $6\%$  Solar, respectively<sup>5</sup>), adopted for the 5–10 Gyr old isochrones, seem to reasonably agree with the RGB colours. For the population younger than 1 Gyr, a higher metallicity of  $Z = 0.006$  appears compatible with the observed CMD (see in particular the RSGs), and also in agreement, within the errors, with spectroscopic oxygen abundance estimates of  $12 + \log_{10}(\text{O/H}) = 8.30 \pm 0.2$  (Magrini & Gonçalves 2009) and  $8.14 \pm 0.08$  (Pilyugin et al. 2014).

Last, in Fig. 5d, we show the  $J_{E,0}$  versus  $Y_{E,0} - H_{E,0}$  CMD of IC 10. Besides the same evolutionary phases already described for the  $H_{E,0}$  versus  $I_{E,0} - H_{E,0}$  diagram (with the exception of the RC, which is fainter than the photometric depth in the NISP bands), we see that NIR CMDs are more effective than optical ones in separating oxygen-rich versus carbon-rich AGB stars (see also, for NGC 6822, Nally et al. 2024, H25), with the former delineating an almost vertical sequence with colours  $0.35 \lesssim Y_{E,0} - H_{E,0} \lesssim 0.55$ , and the latter forming a horizontal feature at  $18.5 \lesssim J_{E,0} \lesssim 20$ . This horizontal feature is considered to be an

<sup>5</sup> We assumed a Solar metallicity of  $Z_{\odot} = 0.0153$  from Caffau et al. (2011). Their solar oxygen abundance estimate is  $12 + \log_{10}(\text{O/H})_{\odot} = 8.76$ .

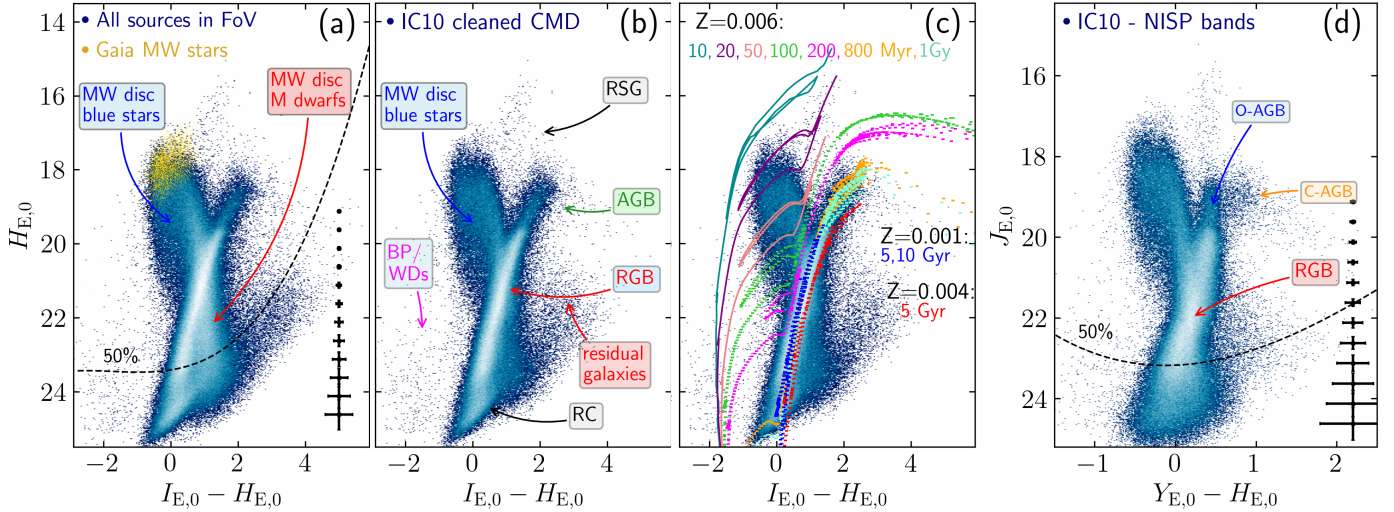


**Fig. 5.** Panel (a):  $H_{E,0}$  versus  $I_{E,0} - H_{E,0}$  reddening-corrected CMD of 336 957 sources with four-band photometry in the entire *Euclid* FoV after selection cuts (see Sect. 2.1). The CMD was corrected for spatially variable reddening as described in Sect. 2.2. Indicated is the contribution from MW disc stars (both blue stars, and red M dwarf stars); yellow dots denote the 7724 MW stars removed from *Gaia* DR3 proper motions and parallaxes. On the right side, we indicate the photometric errors for  $0 \leq I_{E,0} - H_{E,0} \leq 1$ , while the black dashed curve denotes the average 50% completeness level, both from the results of the artificial stars over the entire *Euclid* field. Panel (b): cleaned CMD (227 128 sources) after removal of Galactic M dwarfs and compact red galaxies as described in Sect. 2.3. The main stellar evolutionary sequences are indicated: RSGs with ages from about 20 Myr to 50 Myr; bright and red AGB stars with ages from  $\sim 0.1$  to a few Gyrs; RGB stars, with ages older than 1–2 Gyr; at the faintest magnitudes is a hint of the RC, with ages  $>1$ –2 Gyr. The faint cloud of blue stars at  $I_{E,0} - H_{E,0} \lesssim -1$ ,  $H_{E,0} \gtrsim 22$  is likely dominated by Galactic WDs. Faint red sources at  $I_{E,0} - H_{E,0} \gtrsim 2.5$ ,  $H_{E,0} \gtrsim 21$  are residual background galaxies. Panel (c): same CMD as in (b) with superimposed PARSEC stellar isochrones for a metallicity of  $Z = 0.006$  ( $\sim 40\%$  solar) and ages in the range of 10 Myr–1 Gyr, and for lower metallicities of  $Z = 0.004$  and 0.001 (25%, and 6% solar, respectively) and ages of 5 and 10 Gyr. Panel (d):  $J_{E,0}$  versus  $Y_{E,0} - H_{E,0}$  CMD, where the oxygen-rich and the carbon-rich AGB stars (O-AGB and C-AGB) appear well separated and define vertical and horizontal sequences, respectively. Indicated is the average 50% completeness level and the photometric errors at  $-0.5 \leq Y_{E,0} - H_{E,0} \leq 0.5$ .

effective distance indicator in the near infrared bands (Lee et al. 2025, and references therein).

In all the CMDs, we display the 50% completeness curves and the photometric errors computed through the artificial star tests described in Appendix C.

### 3.1. Distance

The very large sample of well measured IC 10 RGB stars calls for a robust estimate of the distance to the galaxy using one of the most widely used standard candles, the tip of the RGB (TRGB, see, e.g., Lee et al. 1993; Salaris & Cassisi 1998; Madore & Freedman 1995; Bellazzini 2008; Serenelli et al. 2017; Madore & Freedman 2020; Hoyt 2023, and references therein). We can take advantage of the calibration in the  $I_E$  band recently derived by Bellazzini & Pascale (2024, hereafter BP24) using *Gaia* DR3 synthetic photometry (Gaia Collaboration et al. 2023a) of the Small Magellanic Cloud (SMC) and of the Large Magellanic Cloud (LMC). While the minimum dependency of the absolute magnitude of the TRGB on metallicity/colour is achieved in passbands sampling the wavelength range  $\sim 800$ –1000 nm, like the classical Johnson-Cousins  $I$  band, also the broad  $I_E$  band ( $\sim 500$ –930 nm) is well-behaved in the metal-poor range typical of dwarf galaxies (BP24). For instance, BP24 find that the LMC and the SMC differ in  $M_{I_E}^{\text{TRGB}}$  by just  $0.053 \pm 0.072$  mag, in good agreement with theoretical predictions.

The location of the tip of the RGB has been measured with the Bayesian approach described in detail in BP24 and illustrated, for the present application, in Fig. 6. Using the entire IC 10 catalogue, we obtain  $I_{E,0}^{\text{TRGB}} = 21.12 \pm 0.01$ . However, our sample of RGB stars is so rich that we can neglect the inner-

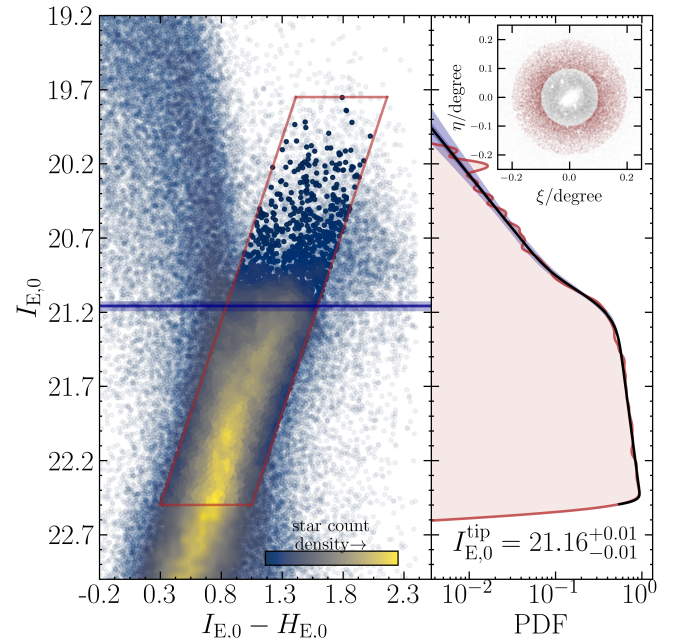


**Fig. 6.** Detection of the TRGB of IC 10 in the annulus  $0.1 \leq R \leq 0.2$ . Left panel: CMD of the considered sample focused on the upper RGB. The red polygon depicts the stars selected for the TRGB detection algorithm, the horizontal line marks the position of the tip, while the purple shaded area encloses the  $\pm 3\sigma$  uncertainty range. Right panel: probability density function (PDF) of the selected sample (red line) with the highest likelihood model superimposed (black line, with  $\pm 3\sigma$  purple shaded area). The mean photometric uncertainties as a function of magnitude are reported in form of errorbars at the right edge of the panel.

most regions of the galaxy where the incompleteness and the crowding are most severe (see Fig. 9 and Appendix C). Thus, for a radial annulus at  $0.1 \leq R \leq 0.2$ , we obtain a clean detection of  $I_{E,0}^{\text{TRGB}} = 21.16 \pm 0.01$  (Fig. 6). From the dataset by Sanna et al. (2008), we measure a mean colour of the TRGB ( $V - I)_0 = 1.822_{-0.12}^{+0.14}$ , compatible with that measured in the LMC by BP24,  $(V - I)_0 = 1.716_{-0.15}^{+0.14}$ . Hence, we adopt as a reference  $M_{I_E}^{\text{TRGB}} = 3.247 \pm 0.050$ , as measured by BP24 for the LMC, obtaining  $(m - M)_0 = 24.41 \pm 0.05$ , corresponding to  $D = 762 \pm 20$  kpc. This is well in the range of the estimates in the literature, listed by Gholami et al. (2025), and, in particular, in good agreement with the recent measures by Sanna et al. (2008), McQuinn et al. (2017b), and Dell'Agli et al. (2018).

## 4. Spatial distribution of stars

In this section, we characterise the spatial distribution of stars in IC 10 and infer the stellar radial profile from individual star counts. This approach is complementary to that previously presented by H25 based on an analysis of the integrated light.

RGB stars were selected from the cleaned, reddening-corrected CMDs presented in Sect. 3. The adopted RGB selection is denoted by the red polygon displayed in Fig. 7a. Fig. 7c displays the resulting RGB star density map derived using 2 arcmin-wide bins and applying a 2D Gaussian smoothing with a standard deviation of 0.2 times the bin size. In the colour bar, the white horizontal line indicates the level of  $3\sigma$  above the average background, computed from an external 6 arcmin size box whose position is indicated on the map. The distribution of the bulk of the old stars appears quite round; with PhotUtils (Bradley et al. 2023), an Astropy package for photometry, we fit elliptical isocontours to the RGB density map. When averaging the derived ellipse parameters for radii less than 20' (black dashed ellipse in Fig. 7), we obtain a centre of  $\alpha \sim 5^\circ 068$ ,  $\delta \sim 59^\circ 301$ , an ellipticity  $e = 1 - b/a = 0.12 \pm 0.02$  and a position angle  $\text{PA} = 0^\circ \pm 10^\circ$ . This ellipticity is lower than that of  $e = 0.31 \pm 0.02$  derived with AutoProf (Stone et al. 2021) from the integrated-light fit, indicating that the old stellar population has a more circular morphology than the young one, which dominates the integrated light. On the other hand, at galactocentric distances larger than  $\sim 20'$ , the distribution of the old stars appears quite asymmetric, with a visible excess toward the north-west direction, where previous studies have identified the presence of a gaseous companion (Nidever et al. 2013; Namumba et al. 2019), and a less prominent excess toward the south-east direction, where a gaseous streamer was identified by Nidever et al. (2013). As shown by the white dashed ellipses in Fig. 7c, this drives a noticeable change in the fitted isocontours' position angle, accompanied by a slight shift of the centres toward the north-west direction, while the ellipticity remains similar. Interestingly, the north-west–south-east elongation derived for the outer stellar component is roughly aligned in the direction of M31 and of the motion of IC 10 with respect to M31 computed from the PMs of Bennet et al. (2024) and Salomon et al. (2021).

As discussed in Sect. 3, the final cleaned CMD from which we select RGB stars still suffers from a non-negligible contamination by MW stars. A non-uniform distribution of foreground contaminants across the imaged FoV could potentially bias our conclusions on the spatial distribution of RGB stars. Indeed, the reddening map in Fig. 4 shows that the foreground extinction is highly variable, with the largest values coinciding with the north-west overdensity revealed by the RGB counts.

We therefore proceed to subtract the contribution of foreground stars from our RGB counts. To this end, we first construct a map of MW contaminants as follows. From the CMD displayed in Fig. 7a, we select bright, blue foreground stars within the golden polygon. This CMD region contains a negligible contribution from IC 10 stars and is therefore effective in tracing the spatial variation of MW stars. The resulting map is then normalized to the mean stellar density computed in the red box region in Fig. 7c, which we assume to be free of RGB stars (see Sect. 4.1). The normalized foreground contamination map is shown in Fig. 7c. The average contamination amounts to  $\sim 12 \pm 1$  stars per arcmin<sup>2</sup>, with a higher density in the north-west quadrant (Q2) than in the south-east one (Q4).

The RGB star count map after subtraction of the variable foreground is displayed in Fig. 7d. Here, the north-west overdensity (and more generally, the elongation from south-east to north-west) remains clearly visible, and perhaps even more pronounced. Ellipse fitting shows no significant change in the innermost regions, while the outer ellipses become even more eccentric than in the uncorrected case. Plots showing the trend of the ellipticity and position angle as a function of semi-major axis are shown in Fig. 8. This analysis thus confirms, and further strengthens, our conclusion that IC 10 hosts an extended, elongated stellar component in its outskirts.

### 4.1. CMD radial trends

In this section, we investigate how different stellar populations are distributed within IC 10 through CMD spatial variations. While we examined the CMDs in concentric annuli of increasing galactocentric distance, using radial steps as small as  $\sim 0.1$  kpc, Fig. 9 presents the CMDs for four representative regions. These regions illustrate how the various stellar populations of IC 10, as well as the foreground MW stars, are distributed across our field of view.

In Fig. 9a, we see that young RSGs (age  $\lesssim 50$  Myr) are confined within an elliptical region with semi-major axis (SMA) less than  $\sim 1.2$  kpc, shown in Fig. 7d as ellipse 1. In this region the incompleteness is severe (see Appendix C), and we only detect the brightest portion of the RGB, together with AGB stars. At larger radii of  $1.2 < \text{SMA} < 3.6$  kpc, between ellipses 1 and 2, the CMD exhibits a well-defined RGB and RC due to stars older than  $\sim 2$  Gyr, and a conspicuous population of intermediate-age AGB stars as old as  $\sim 0.1$ –2 Gyr (Fig. 9, panel b). At larger distances of  $3.6 < \text{SMA} < 5.8$  kpc, between ellipses 2 and 3, few AGB stars are observed, and the IC 10 stellar population mostly consists of old RGB plus RC stars (Fig. 9, panel c). At these radii, the contribution of MW foreground stars compared to stars in IC 10 is relatively high, and the brightest part of the RGB can hardly be recognized. Nonetheless, the depth of *Euclid* photometry is such that the faintest portion of the RGB at  $H_{E,0} \sim 22$  and the RC are clearly detected. The radial distribution of the stellar populations is in agreement with the spatial maps presented by H25, showing an increasing segregation of stars toward the galaxy centre with decreasing age.

Finally, panel (d) of Fig. 9 shows that the CMD extracted in the external region corresponding to the red box in Fig. 7c is dominated by MW foreground stars, with evidence for a marginal, if any, population of RGB/RC stars in IC 10. This is best highlighted in Fig. 9, panel (e), where these stars are plotted on top of the  $1.2 < \text{SMA} < 3.6$  kpc CMD. Despite the fact that bright RGB stars are absent in the outer region, we notice a few stars fainter than  $H_{E,0} \sim 22$  that could potentially be RGB/RC

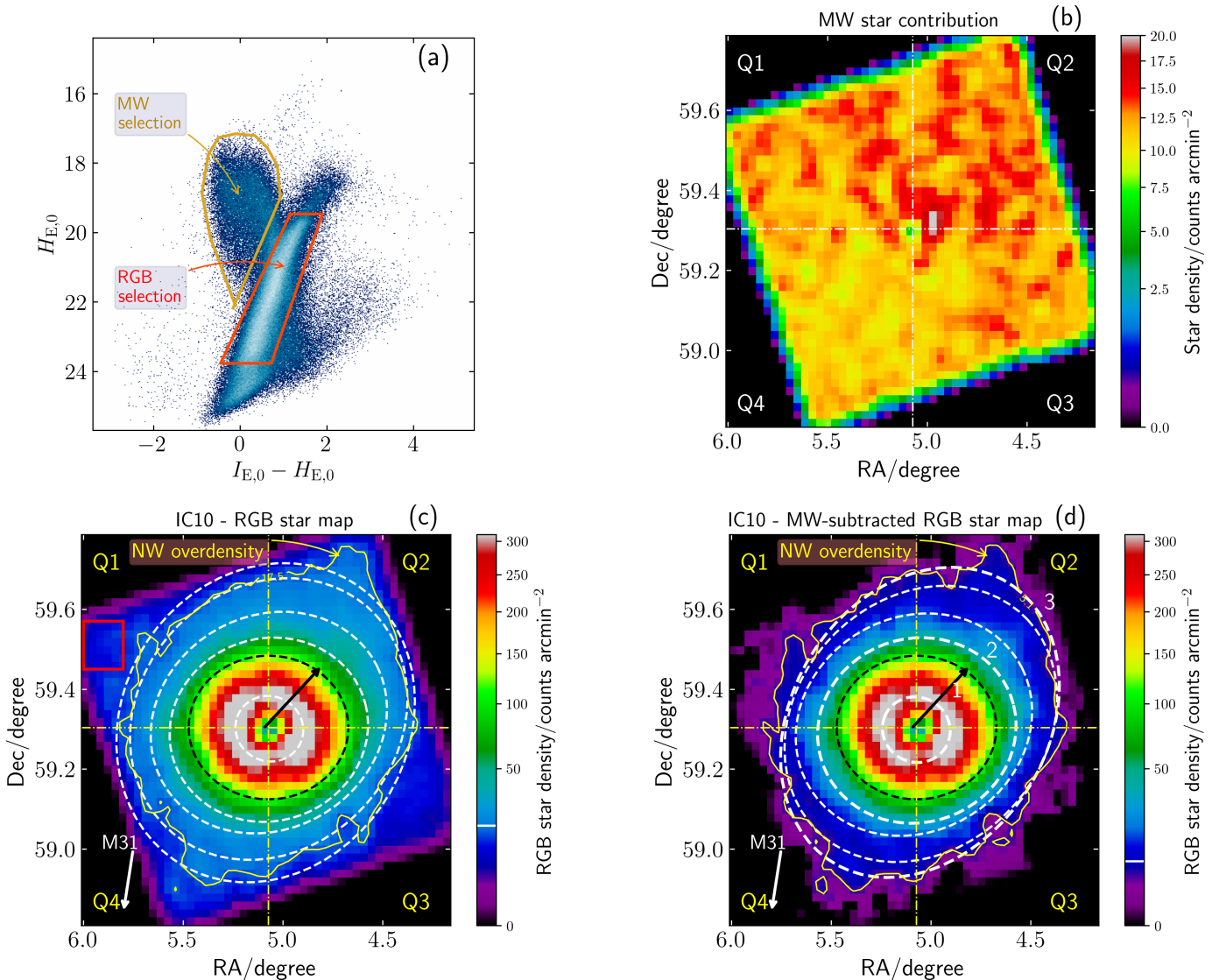


**Fig. 7.** Panel *a*: cleaned, reddening-corrected  $H_{E,0}$  versus  $I_{E,0} - H_{E,0}$  CMD of IC 10. The red and golden polygons denote our selection of RGB stars and bright MW foreground stars, respectively. Panel *b*: spatial density map, in units of counts per arcmin $^2$ , of the contribution from foreground MW stars to the RGB counts. Panel *c*: spatial density map of sources within the red polygon of panel *(a)*, containing both RGB stars and MW stars. In the right-hand colour bar, the horizontal white segment denotes  $3\sigma$  above the background computed from the counts in the region outlined by the red box. The black dashed ellipse with  $e = 0.12$  and  $PA = 0^\circ$  provides a good fit to the bulk of the old stellar population out to a radius  $\lesssim 20'$ . The most external white dashed ellipses highlight the change in position angle and ellipticity driven by a star count excess in the north-west direction, and by a less prominent excess in the south-east direction. The isodensity contour at  $2\sigma$  above the background is in yellow. The RGB density drop in the most central galaxy region is due to high incompleteness. Q1 to Q4 denote the location of the four quadrants described in Sect. 4.2. The white arrow indicates the direction of M31, while the black arrow is the direction of IC 10's velocity with respect to M31 projected on the sky. Panel *d*: same as in *(c)*, but after subtracting the contribution from MW stars represented in *(b)*. Ellipses 1–2–3 correspond to the regions selected for the CMD spatial analysis in Fig. 9.

stars in IC 10, although this population is highly subdominant compared to MW stars.

Although deeper data reaching fainter evolutionary phases (such as the old MS turnoff) would be required to confirm the presence there of a very diffuse stellar component associated with IC 10, our analysis indicates that, for the purposes of this study, it is reasonable to assume that this outer region is devoid of IC 10 stars. It therefore traces the contribution of foreground MW stars and background galaxies to the IC 10 point-source photometry.

#### 4.2. Resolved star count profile

We inferred the resolved stellar profile of IC 10 by computing the number density of RGB stars in 0.25 kpc-width elliptical annuli with increasing galactocentric distance, adopting the ellipse parameters of  $e = 0.12$  and  $PA = 0^\circ$  derived for the bulk of the stellar population in Fig. 8. RGB stars were selected from the reddening-corrected CMD, but completeness corrections, as derived in Appendix C, were applied to the observed, uncorrected magnitudes. For each annulus, we binned the RGB stars in intervals of 0.5 mag in the  $I_E - H_E$  colour and 0.5 mag in  $H_E$ , computed the counts in each bin, and then divided them by the completeness of the corresponding colour-magnitude bin computed in the

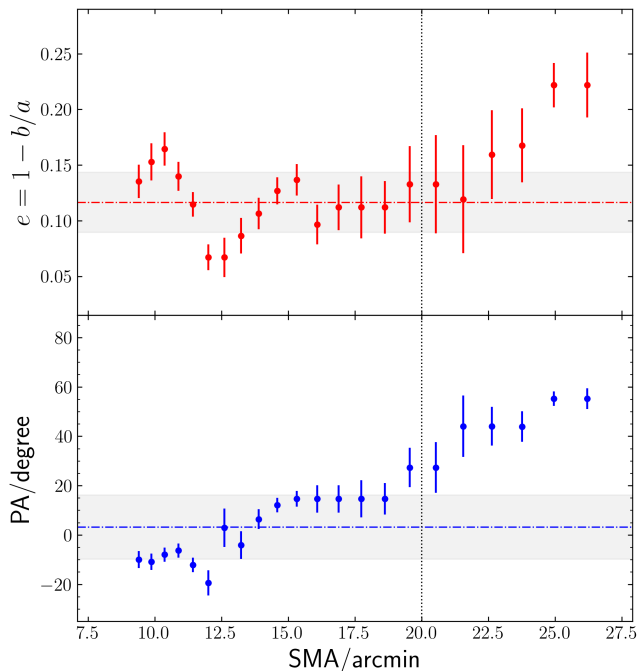


**Fig. 8.** Top panel: ellipticity as a function of semi-major axis resulting from ellipse fitting to the RGB star density map in Fig. 7d. The horizontal line and the shaded area denote the average value of  $e = 0.12 \pm 0.02$  derived from the ellipses at  $\text{SMA} \lesssim 20'$ . Bottom panel: same as top, but for the PA, measured from north to east counter-clockwise, with the minor axis oriented north-south. The horizontal line and shaded area correspond to an average value of  $\text{PA} = 0^\circ \pm 10^\circ$ .

same annulus. The final counts were then computed as the sum of the corrected counts in all the bins. Errors on the profile were derived accounting for both the Poissonian  $\sqrt{N}$  error on the observed number of star counts (which is the dominant component) and the uncertainty on the completeness fraction, estimated as  $\sqrt{N_{\text{out}}}/N_{\text{inp}}$ , where  $N_{\text{inp}}$  and  $N_{\text{out}}$  are, for each colour-magnitude bin, the number of injected and recovered artificial stars, respectively.

Given the severe incompleteness toward the inner galaxy regions, as evident in Fig. 9a and Fig. C.2, we adopted for the most internal stars a brighter RGB selection than the one outlined by the polygon in the top panel of Fig. 7 and considered only the portion of the RGB with  $H_{\text{E},0} \lesssim 21.5$  (see Smercina et al. 2023, for a similar approach). Despite their different absolute values, the bright-limit and faint-limit RGB profiles share a common slope in a region at  $1.9 \lesssim \text{SMA} \lesssim 2.6$  kpc, which we adopted to normalise the bright profile to the faint one. Eventually, the final merged profile results from the combination of the bright-limit one at  $\text{SMA} \lesssim 1.9$  kpc and the faint-limit one at larger radii. The profile was sampled out to a semi-major axis of  $\text{SMA} \sim 35'$ , or  $\sim 7.7$  kpc. At  $\text{SMA} \gtrsim 24'$ , increasingly smaller fractions of the elliptical annuli are covered by the *Euclid* FoV, implying poor statistics at the largest galactocentric distances.

Besides the total profile, we also computed profiles for four different quadrants departing from IC 10's centre, as indicated in Figs. 7c and 7d: Q1 to the north-east, Q2, to the north-west, Q3 to the south-west, and Q4 to the south-east. The results are displayed in the top panel Fig. 10, where both the total and partial RGB count profiles are shown as a function of the semi-major axis. The partial profiles are seen to be in very good agreement with each other at  $\text{SMA} \lesssim 20'$ . However, at larger radii, the Q1 and Q3 profiles fall below the Q2 and Q4 ones, in agreement

with the north-west overdensity and the preferential distribution of RGB stars along the north-west–south-east direction in the map of Fig. 7d. It is difficult to explain these differences with the uncertainties associated with the star count profiles, as shown by the error bars in Fig. 10. The horizontal line indicates the contribution from MW foreground stars and unresolved background galaxies, computed as the average density from the map in Fig. 7b, while the shaded area is its standard deviation. Eventually, we subtracted this contribution from the total RGB profile.

The background-subtracted star count profile was normalised to surface brightness units by anchoring it to the  $H_{\text{E}}$ -band integrated-light profile inferred with *Autoprof*. More specifically, *Autoprof* was run on the  $H_{\text{E}}$  image forcing the elliptical isophotes to have the same centre, ellipticity and position angle as those adopted to derive the RGB star count profile. The  $H_{\text{E}}$  band was chosen as more sensitive than the bluer bands to the old stellar component (see however H25, for a comparison with the profiles in the other *Euclid* bands). We corrected the profile adopting  $E(B - V) = 0.8$ , corresponding to the median reddening value over the *Euclid* FoV. The normalization of the resolved star-count profile to the integrated-light one was performed in the region at  $1.5 \lesssim \text{SMA} \lesssim 2.5$  kpc, where the CMD spatial analysis indicates negligible contribution from young stars (see also Sanna et al. 2010) and the slopes of the integrated-light and resolved RGB star profiles are in excellent agreement.

At  $\text{SMA} \lesssim 1$  kpc, the integrated-light profile exhibits a rapid steepening, as expected from the increasingly large contribution of young, luminous stars, or even old, highly crowded stars. Here, we are not able to robustly trace the RGB profile because of the severe incompleteness toward the galaxy centre. At  $\text{SMA} \gtrsim 3$  kpc the integrated-light profile flattens out, reaching the  $1\sigma$  surface brightness limit from H25, due to the impossibility of properly removing foreground star and background galaxy contaminants. On the other hand, the RGB star count profile keeps decreasing down to  $\sim 29$  mag arcsec $^{-2}$  in  $H_{\text{E},0}$  (reddening corrected). Our final calibrated profile is shown in the bottom panel of Fig. 10.

We fitted Sérsic and exponential profiles to the RGB star profile following the procedure by Sánchez-Alarcón et al., in prep. For a single Sérsic component, we found best-fit parameters of  $\mu_{\text{e},H} = 22.14$ ,  $n = 1.5$  and  $r_{\text{e}} = 1.0$  kpc. This best-fit model is shown with a red solid line in panel (a) of Fig. 11. Although the observed RGB counts are in good agreement with the fitted profile at  $\text{SMA} \lesssim 5$  kpc, they appear to be systematically above the model at larger radii. This is best illustrated in panel (b) of Fig. 11, showing the surface brightness residuals from the observed profile and the best-fit Sérsic model. This indicates the presence of a second component that dominates in the outer regions. To compensate for this extended emission, we fitted a two-component model, with a Sérsic profile and an exponential disc (equivalent to a Sérsic with  $n = 1$ ). The two-component model, shown with the dashed blue line in Fig. 11, is able to reproduce both the internal and external regions at  $\text{SMA} \gtrsim 5$  kpc, as evident from the residuals in panel (b). The parameters of the one- and two-component best-fit models are listed in Table 1. In addition to the parameters of the fit (i.e. the Sérsic index  $n$ , the effective radius  $r_{\text{e}}$ , the effective surface brightness  $\mu_{\text{e},H}$ , the central surface brightness  $\mu_{0,H}$  and the scale height  $h$  of the exponential disc component), we provide the reddening-corrected  $H_{\text{E},0}$ -band magnitude in the individual components, the total  $H_{\text{E},0}$  magnitude from both components, the stellar mass of the individual components, and the total stellar mass. The  $H_{\text{E},0}$ -band magnitudes were obtained by integrating the profile to a

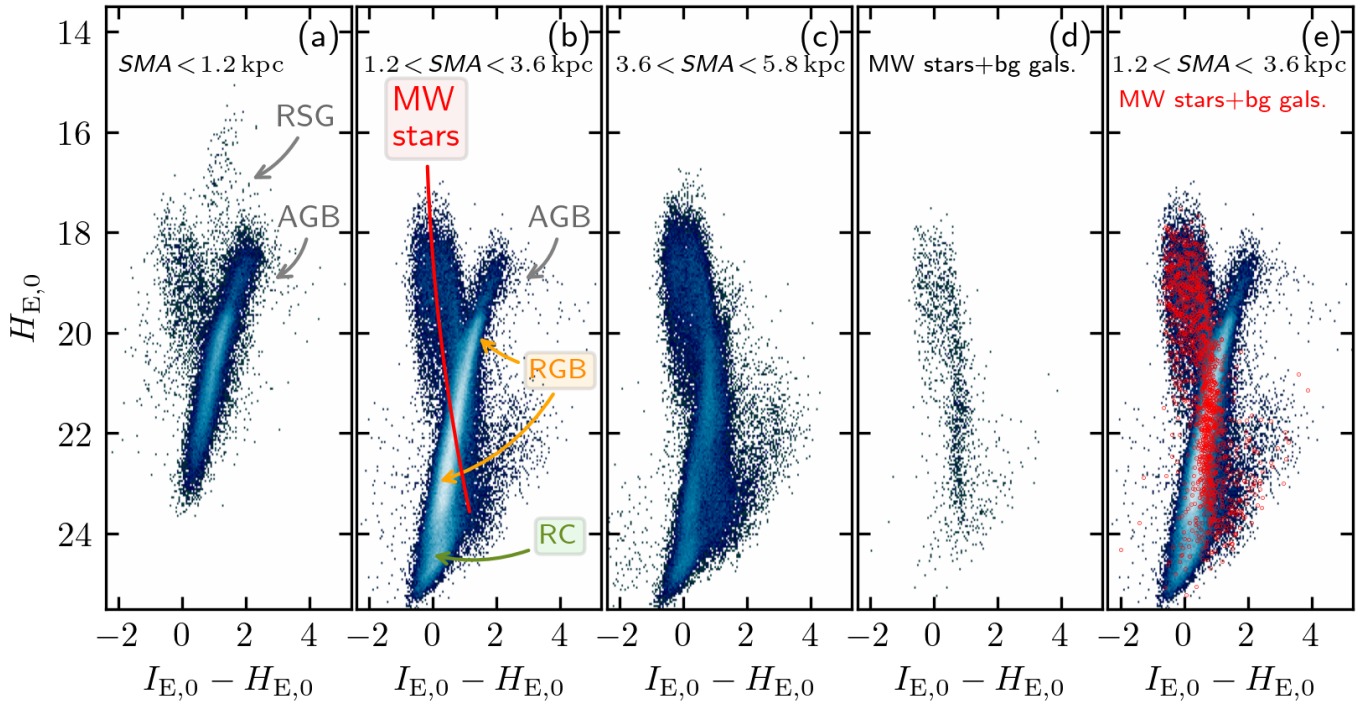


**Fig. 9.**  $H_{E,0}$  versus  $I_{E,0} - H_{E,0}$  reddening-corrected CMD for four regions in IC 10 at different galactocentric distances: one within ellipse 1 in Fig. 7d, at semi-major axis  $SMA < 1.2$  kpc (panel a), showing both RSG stars and AGB stars, but only the brightest portion of the RGB due to severe incompleteness; one between ellipses 1 and 2, at  $1.2 < SMA < 3.6$  kpc (panel b), showing a well defined RGB and RC, AGB stars, but no young RSG; a more external one between ellipses 2 and 3, at  $3.6 < SMA < 5.8$  kpc (panel c), with no RSG and almost no AGB stars; an external region (panel d), corresponding to the red box in Fig. 7c, sampling MW stars and background galaxies, and appearing almost free of stars in IC 10. Panel (e) displays the CMD of panel (b) with the stars in panel (d) overplotted in red. The red curve in panel (b) describes the position of residual MW foreground stars not removed by our selections in Sect. 2.3.

radius of 50 kpc, so that the outer wings of the profile are fully included; specifically, this radius was chosen such that the integrated magnitude changes by less than 0.1%, well below the uncertainty of the profile. The stellar mass in the various components was computed by adopting a stellar mass-to-light ratio in the  $H$  band of  $\Upsilon_H \sim 1.16$ , derived from the PARSEC<sup>6</sup> simple stellar populations (SSPs) for  $Z = 0.001$  and a canonical two-part-power law initial mass function from Kroupa (2001, 2002) and Kroupa et al. (2013), corrected for unresolved binaries; SSPs of different ages were weighted according to the star formation history inferred by Weisz et al. (2014) at look-back times  $\gtrsim 1$  Gyr, and then linearly combined. We adopted an  $H$ -band AB magnitude of  $M_{H,\odot} = 4.66$  for the Sun from Willmer (2018). To account for the uncertainty in mass due to the metallicity dependence, we computed the mass-to-light ratio for two extreme metallicity values of  $Z = 0.0004$  and  $Z = 0.004$ , obtaining  $\Upsilon_H \sim 1.3$  and  $\sim 1.0$ , respectively. This eventually results into a stellar mass of  $M_\star = 6.7_{-0.9}^{+0.9} \times 10^8 M_\odot$ , which is a lower limit since it does not account for the amount of mass in stars younger than 1 Gyr.

At the largest sampled galactocentric distances, the most important source of uncertainty in the profile is the adopted contribution from MW foreground stars, vastly dominating over unresolved background galaxies at IC 10’s Galactic latitude. Thus, as a consistency check, we computed the number density of MW stars predicted by TRILEGAL that fall within the RGB selection polygon displayed in the top panel of Fig. 7. More specifically,

TRILEGAL was run assuming no dust extinction, but then applying to the simulated CMD in the *Euclid* filters an average extinction of  $A_{I_E} = 1.7$  and  $A_{H_E} = 0.4$ , consistent with the average reddening value inferred in Sect. 2.2. This provides a density of  $\sim 8 \pm 1$  stars per arcmin<sup>2</sup>, where the error accounts for the spread in reddening, to be compared with an average density of  $\sim 12 \pm 1$  stars per arcmin<sup>2</sup> computed from the map in Fig. 7b. Since the TRILEGAL computation does not account for the contribution of unresolved background galaxies, this value should be considered as a lower limit. From other ERO Showcase data with low contamination from the MW disc, we estimate that unresolved background galaxies contribute less than 10% of the MW star contamination.

The profile and the fits resulting from the subtraction of the TRILEGAL background value are shown in panel (c) of Fig. 11, while the residuals are displayed in panel (d). A one-component Sérsic fit results into  $\mu_{e,H} = 22.14$ ,  $n = 2.0$  and  $r_e = 1.0$  kpc which, as in the previous case, is unable to reproduce the counts at  $SMA \gtrsim 5$  kpc, indicating the presence of an additional, more extended stellar component. We thus fitted a two-component model, with a Sérsic and an exponential disc, finding again that this is able to reproduce the profile both in the inner and in the outer regions. The results of the fit are given in Table 1.

## 5. Discussion

From resolved stellar photometry in the *Euclid*  $I_E$ ,  $Y_E$ ,  $J_E$ , and  $H_E$  bands we have characterised the extended, low surface brightness, old stellar component of IC 10 out to a radius of  $\sim 35'$  ( $\sim 8$  kpc, for our distance estimate of  $\sim 0.76$  Mpc) from

<sup>6</sup> These can be downloaded via the web page <https://stev.oapd.inaf.it/cgi-bin/cmd>

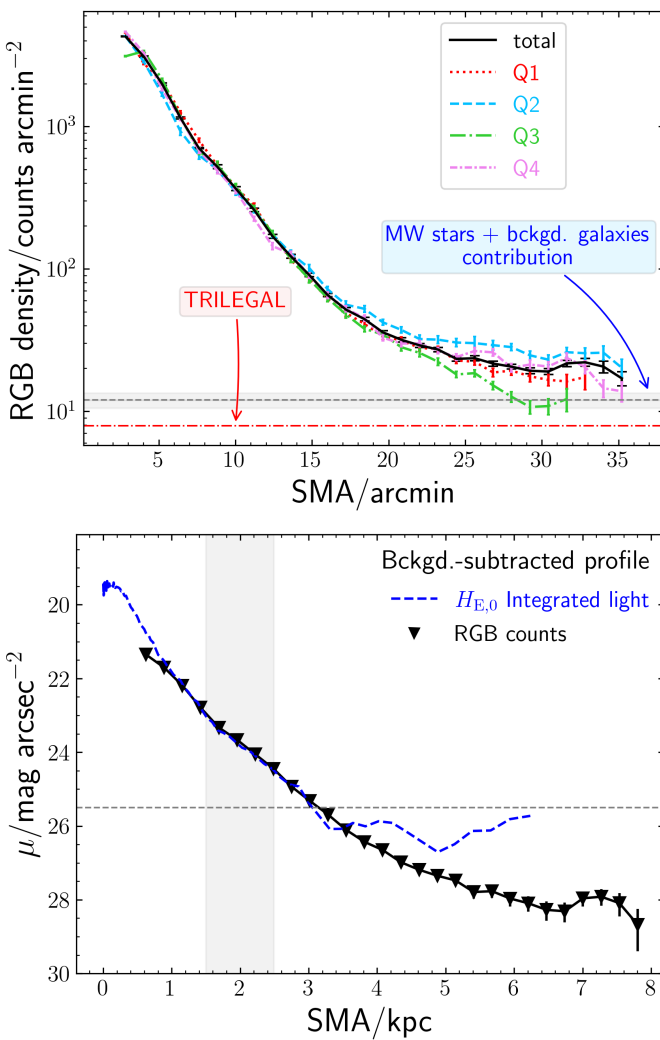


**Fig. 10.** Top panel: RGB count density in units of number of counts per  $\text{arcmin}^2$  as a function of semi major-axis. The solid black line is the total profile, while the coloured dashed/dotted lines correspond to the profiles in four different quadrants: Q1 (north-east), Q2 (north-west), Q3 (south-west), and Q4 (south-east). The horizontal dashed line is the average contribution from MW stars plus background galaxies directly inferred from our data (see Sect. 7), while the shaded area is the  $\pm 1$  standard deviation region. The dotted-dashed line is instead the MW contribution predicted by TRILEGAL. Bottom panel: RGB profile in  $\text{mag arcsec}^{-2}$  (black triangle symbols) after subtraction of the foreground and background contaminants corresponding to the horizontal dashed line in the top panel. The profile was normalised to the reddening-corrected, integrated-light profile from Autoprof (dashed blue line) in the region indicated by the shaded area. The dashed horizontal line is the  $1\sigma$  surface brightness limit from Autoprof in H25.

the galaxy centre, corresponding to about 5 times the  $\mu_B = 25 \text{ mag arcsec}^{-2}$  isophotal radius (de Vaucouleurs et al. 1991). This was achieved by selecting RGB stars in the reddening-corrected  $H_{\text{E},0}$  versus  $I_{\text{E},0} - H_{\text{E},0}$  CMD, after subtracting the contribution of unresolved background galaxies and MW foreground stars. Thanks to the wide field of view and superb spatial resolution of *Euclid*, this is the first time the stellar component of IC 10 has been studied to such large radii and to (reddening-corrected) surface brightness levels as faint as  $\mu_{H_{\text{E}}} \sim 29 \text{ mag arcsec}^{-2}$ .

A previous study by Demers et al. (2004) identified RGB stars out to  $\sim 16'$ , while Tikhonov & Galazutdinova (2009) reported a thick disc with dimensions  $14.5' \times 10.5'$  (semi-major

**Table 1.** Structural properties of the old stellar component in IC 10.

Single Sérsic Model			
Parameter	Unit	Direct Bckgd.	TRILEGAL Bckgd.
$\mu_{\text{e},H}$	$\text{mag arcsec}^{-2}$	22.14	22.14
$r_{\text{e}}$	kpc	1.0	1.0
$n$	—	1.5	2.0
Sérsic + Exponential Disc Model			
Parameter	Unit	Direct Bckgd.	TRILEGAL Bckgd.
$\mu_{\text{e},H}$	$\text{mag arcsec}^{-2}$	22.04	22.06
$r_{\text{e}}$	kpc	1.0	1.0
$n$	—	1.0	1.1
$\mu_{0,H}$	$\text{mag arcsec}^{-2}$	25.91	26.59
$h$	kpc	3.2	6.8
$H_{\text{E,Sérsic}}$	mag	7.32	7.29
$H_{\text{E,exp}}$	mag	9.35	8.43
$H_{\text{E,tot}}$	mag	7.16	6.96
$M_{\star,\text{Sérsic}}$	$M_{\odot}$	$5.8_{-0.8}^{+0.7} \times 10^8$	$6.0_{-0.8}^{+0.8} \times 10^8$
$M_{\star,\text{exp}}$	$M_{\odot}$	$0.9_{-0.1}^{+0.1} \times 10^8$	$2.1_{-0.3}^{+0.3} \times 10^8$
$M_{\star,\text{tot}}$	$M_{\odot}$	$6.7_{-0.9}^{+0.9} \times 10^8$	$8.1_{-1.1}^{+1.0} \times 10^8$

Notes. All listed values are obtained assuming an average  $E(B-V) = 0.8$  and  $D = 0.762 \text{ Mpc}$  (Sect. 3.1). The symbols  $\mu_{\text{e},H}$ ,  $r_{\text{e}}$ , and  $n$  correspond to the following Sérsic fit parameters: reddening-corrected surface brightness at  $r_{\text{e}}$ , effective radius, and Sérsic index, respectively. The exponential disc parameters – central surface brightness and scale height – are  $\mu_{0,H}$  and  $h$ . The quantities  $H_{\text{E,Sérsic}}$ ,  $H_{\text{E,exp}}$ , and  $H_{\text{E,tot}}$  are the apparent, reddening-corrected magnitudes in the  $H_{\text{E}}$  band for the Sérsic, disc, and total components.  $M_{\star}$  represents the stellar mass in old ( $\gtrsim 1 \text{ Gyr}$ ) stars for all components, with the errors reflecting the uncertainty in metallicity. Values are provided for the two cases of the background directly estimated from the counts in an outer region of IC 10 (Direct Bckgd.) and of the background inferred from the TRILEGAL Galactic model (TRILEGAL Bckgd.).

times semi-minor axis). From Suprime-Cam Subaru data, Sanna et al. (2010) detected sizable samples of RGB stars out to radial distances of  $18' - 23'$  from the galactic centre and argued, based on predictions for the foreground contamination from Galactic models, that IC 10 stars may extend as far as  $\sim 34' - 42'$ . Using optical and NIR wide-field imaging with MegaCam and the Wide Field Camera at the CFHT and UKIRT telescopes, respectively, Gerbrandt et al. (2015) traced the old stellar population of IC 10 out to a radial distance of  $\sim 20'$ . However, all these studies achieved shallower surface brightness depths than our current analysis. While their CMDs were limited to the upper  $\sim 1.5 - 3$  magnitudes of the RGB, our reddening corrected photometry probes down to  $H_{\text{E},0} \gtrsim 24$ , i.e.  $\sim 4$  magnitudes below the RGB tip. Indeed, our CMD spatial analysis (see Sect. 4.1 and Fig. 9) highlights how critical CMD depth is for detecting low-density stellar components; beyond  $\text{SMA} \gtrsim 3.6 \text{ kpc} (\gtrsim 16')$ , nearly no RGB stars would be seen if we were limited to the top  $\sim 2$  mag of the RGB. Our results demonstrate that IC 10's stellar component is significantly more extended than previously thought: RGB stars are still detected at the edge of the *Euclid* FoV, suggesting the galaxy could extend nearly as far as the enormous  $62' \times 80'$  H<sub>1</sub> envelope found by Huchtmeyer (1979). Other studies have shown that when traced down to very low surface brightness levels, the stellar component of galaxies can be as extended as the H<sub>1</sub> distribution (Bellazzini et al. 2014; Annibali et al. 2020; Mancera Piña et al. 2024).

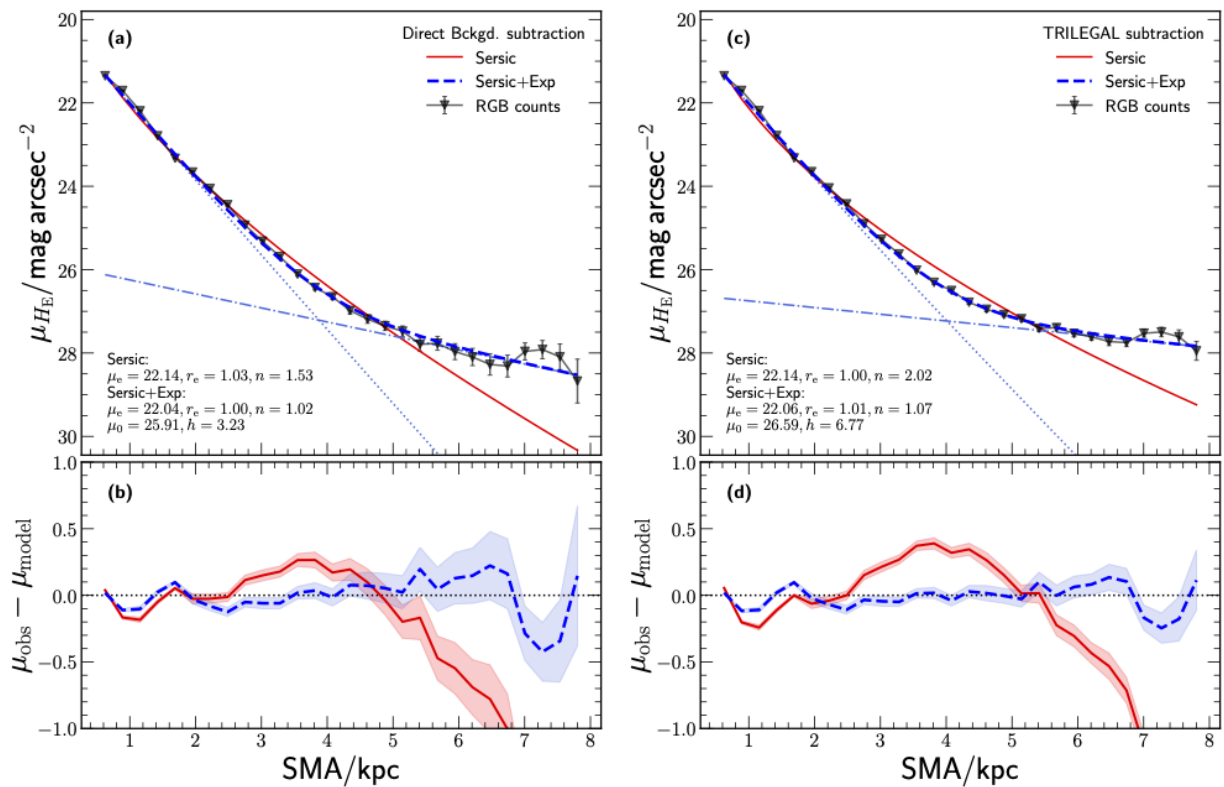


**Fig. 11.** Background-subtracted RGB profiles (black triangle symbols) normalised to the  $H_{E,0}$  integrated-light profile. In *panel (a)* the profile was obtained by subtracting the background (MW stars plus compact background galaxies) estimated from the star counts at large radii, while in *panel (c)* the contribution from MW stars was inferred from TRILEGAL. In both panels, the solid red line is the best-fit Sérsic model. The dashed blue line is instead the fitted two-component model consisting of a Sérsic profile (dotted red line) and an exponential disc (dot-dash blue line). *Panels (b)* and *(d)* display the residuals in surface brightness for the one and two-component best-fit models.

The RGB star count map reveals a round and regular morphology within a radius of  $\sim 20'$ , consistent with Gerbrandt et al. (2015). In this region, the star count map is well fitted with iso-density contours characterised by ellipticity  $e \sim 0.12$  and position angle  $\text{PA} \sim 0^\circ$ . However, at larger radii, the isocontours begin to twist, driven by an excess of stars to the north-west and a less prominent excess to the south-east (see Sect. 4). Similar features have been observed in tidally disturbed dwarf galaxies (e.g., Golini et al. 2024). Indeed, the north-west overdensity is in the same direction where Nidever et al. (2013) identified the  $1.3^\circ$  long  $\text{H}\alpha$  feature (corresponding to  $\sim 17$  kpc at a distance of 0.76 Mpc), culminating in a high-density clump later confirmed by Namumba et al. (2019). As introduced in Sect. 1, this structure was interpreted as the result of a recent interaction or merger with a companion dwarf galaxy, a scenario that, according to Ashley et al. (2014), could also explain other peculiar morphological and kinematical properties of the gas in IC 10: the southern plume, the three spurs, and the outer  $\text{H}\alpha$  region counter-rotating with respect to the inner gaseous disc (Shostak & Skillman 1989; Wilcots & Miller 1998). We may now be detecting, for the first time, a stellar counterpart to this accretion event.

However another intriguing possibility is that the north-west–south-east elongated stellar component results from a tidal interaction with M31. Using PMs, Bennet et al. (2024) derived the orbital history of IC 10 and found that the galaxy underwent pericentric passage with M31 about 1 Gyr ago and that it is still inside its virial radius. The alignment of the elongated stellar feature that we infer through RGB counts with the orbit of IC 10 around M31 (Nidever et al. 2013; Bennet et al. 2024), together

with a marked flattening of the outer density profile (see discussion below), is suggestive of a tidal origin (e.g., Johnston et al. 1999; Muñoz et al. 2008).

As our current *Euclid* coverage does not extend to the full extent of either the stellar or the  $\text{H}\alpha$  component of IC 10, data from a larger field-of-view than is currently available would be required to clarify the nature of the outer elongated stellar emission, and to determine whether it originates from tidal interaction with M31 or instead represents the stellar counterpart of the extended  $\text{H}\alpha$  feature thought to result from the accretion of a smaller satellite.

We derived the radial profile of the old ( $\gtrsim 1$ –2 Gyr) stellar component in IC 10 from RGB star counts, corrected for incompleteness through artificial-star experiments. The global contribution from compact background galaxies and, predominantly, foreground MW stars was subtracted using an external region assumed to be free of IC 10 members, while accounting for spatial variations in MW star density across the field. The RGB star density was then converted to surface brightness ( $\text{mag arcsec}^{-2}$ ) by scaling to the  $H_E$ -band integrated-light profile, following a method widely used in studies of resolved stellar systems (e.g. Bellazzini et al. 2011; Ryś et al. 2011; Bernard et al. 2012; Bellazzini et al. 2014; Kniazev et al. 2009; Annibali et al. 2020; Higgs et al. 2021). The reddening-corrected surface brightness profile reaches  $\mu_{H_E} \sim 29 \text{ mag arcsec}^{-2}$ .

The dominant uncertainty arises from the correction for background and foreground contamination, which critically affects the profile in the galaxy outskirts, where low surface brightness values are highly sensitive to small subtraction errors. Our CMD analysis indicates that a few RGB stars from IC 10 are still

present near the edge of the *Euclid* FoV, implying that we may be slightly oversubtracting the background. For comparison, the TRILEGAL model predicts a foreground density about 30% lower than our empirical estimate, yielding a flatter outer profile. Contamination from unresolved background galaxies is insufficient to explain this discrepancy, as their contribution is estimated to be  $< 10\%$  of that from MW stars, based on other ERO datasets. Given these uncertainties, the true IC 10 profile likely lies between the two profiles obtained under different subtraction assumptions (e.g., see [Martin et al. 2008](#); [McMonigal et al. 2014](#); [Collins et al. 2021](#), for similar challenges).

The stellar density profile of dwarf galaxies retains the imprint of both internal and environmental evolutionary processes (e.g., [Martin et al. 2025](#)). Departures from a single Sérsic component, due to an excess of stars at large radii, can signal the action of galactic tides from interactions with a more massive host, which are expected to redistribute stars and produce extended outer envelopes ([Peñarrubia et al. 2009](#); [Łokas et al. 2013](#)). Alternatively, diffuse outskirts may arise from dwarf-dwarf encounters or mergers (e.g. [Deason et al. 2022](#)), or more generally from the gradual build-up of a stellar halo through the accretion of low-mass companions over cosmic time ([Cooper et al. 2025](#); [Celiz et al. 2025](#)).

We fitted the surface brightness profile of IC 10 with Sérsic models. A single-component model with  $n = 1.5\text{--}2$  (depending on the adopted profile) reproduces the inner profile. However, at radii larger than about 5 kpc, we observe a significant excess with respect to the Sérsic model. This indicates the presence of a second component dominating the galaxy outskirts. Nevertheless, given that it is virtually impossible to trace its entire extension with the data in hand makes its modelling quite uncertain. With these limitations in mind, we adopted a two-component model comprising a Sérsic plus an exponential profile. The inner Sérsic component is well-constrained, with  $n \sim 1.0\text{--}1.1$ ,  $r_e \sim 1$  kpc, and  $\mu_e \sim 22\text{--}22.1$  mag arcsec $^{-2}$  (thus insensitive to which of the two profiles is adopted). Our Sérsic index is in good agreement with that derived from RGB counts by [McQuinn et al. \(2017a\)](#), and somewhat larger than the value of  $n = 0.75 \pm 0.06$  previously inferred by [Gerbrandt et al. \(2015\)](#), while our effective radius is smaller than their  $r_e \sim 1.2$  kpc. On the other hand, the exponential component shows greater sensitivity to which of the two profiles is adopted, with central surface brightness values in the range of  $\mu_0 \sim 25.9\text{--}26.6$  mag arcsec $^{-2}$  and a scale height in the range of  $h = 3.2\text{--}6.8$  kpc, where the larger value of  $h$  is associated with the flatter profile. From the results of the fit, we infer a total reddening corrected magnitude in the range of  $H_{\text{tot}} \sim 7.0\text{--}7.2$ , from which we derive a stellar mass of  $M_\star = (6.7\text{--}8.1) \times 10^8 M_\odot$  in stars older than  $\sim 1$  Gyr. According to the star formation history derived by [Weisz et al. \(2014\)](#), stars in this age range contribute at least 95% of the total stellar mass in IC 10. Our mass estimate is larger than the value of  $\sim 4 \times 10^8 M_\odot$  inferred from integrated light by [Lee et al. \(2003\)](#) and [Nersesian et al. \(2019\)](#).

Our structural parameters are consistent with scaling relations of effective radius and effective surface brightness versus magnitude for dwarf galaxies (e.g., [McConnachie 2012](#)). The inner Sérsic index  $n \sim 1$  agrees with values reported from previous studies of dwarf irregulars based on integrated-light photometry down to  $\mu \sim 26$  mag arcsec $^{-2}$ . From  $H$ -band data, [Kirby et al. \(2008\)](#) derived  $0.6 \lesssim n \lesssim 1.8$  for dwarf irregular galaxies within  $\sim 10$  Mpc distance, while [Young et al. \(2014\)](#) found  $1 \lesssim n \lesssim 2$  for nearby dwarfs with luminosity similar to IC 10; from  $g$ -band photometry, [Poulain et al. \(2021\)](#) found values of  $0.6 \lesssim n \lesssim 1.4$  for dwarf irregulars with  $M_g < -14$ . However, these compar-

isons are limited by the shallower depth of these studies, which typically miss the low-density outskirts explored here.

Studies of the extended stellar component of dwarf galaxies down to  $\mu_V \sim 30\text{--}31$  mag arcsec $^{-2}$  have been presented for some nearby objects based on a resolved star approach. [Bellazzini et al. \(2014\)](#) derived the RGB star count profiles of the dwarf irregulars Sextans A and B and found both galaxies to extend for  $\sim 4$  kpc from their centres along their major axes. Both profiles show significant changes of slope that can not be reproduced with single Sérsic models, with Sextans A exhibiting an external flattening at galactocentric distances larger than  $\sim 2.5$  kpc likely due to the presence of a tidal tail. On the other hand, other dwarfs are well fitted by single Sérsic models, like UGC 4879 ( $n = 1.3$ , [Bellazzini et al. 2011](#)), NGC 6822 ( $n = 1$ , [Zhang et al. 2021](#)), Sagittarius ( $n = 1$ , [Beccari et al. 2014](#)), and Phoenix ( $n = 0.8$ , [Battaglia et al. 2012](#)). [Higgs et al. \(2021\)](#) presented an extensive study of structural parameters from RGB count profiles in 12 nearby dwarfs (IC 10 is not included in their sample). They found the majority of dwarfs to be more suitably described by single component Sérsic models with  $n \sim 0.4\text{--}1.3$ , with the exception of UGC 4879, DDO 210, and WLM for which the preference between one or two components is less clear. Their study shows no extended stellar substructure, which could be signs of a recent merger or accretion of satellites, to be present in any of the studied galaxies. It remains an open question whether IC 10 represents a rare case of an exceptionally extended stellar envelope, due to a recent merger history with a smaller companion or to its interaction with M31, or whether such features are common in dwarfs but have largely gone undetected due to the lack of imaging that combines both sufficient depth and wide spatial coverage.

In the context of a scenario where the extended stellar population of IC 10 traces its hierarchical assembly history, the inferred properties provide an opportunity to confront with the predictions from  $N$ -body simulations of dwarf galaxies in a  $\Lambda$ CDM cosmological framework. According to simulations, the typical stellar mass fraction accreted by an IC 10 mass-like galaxy is below 10%, although this fraction can be as high as 100% in some cases (e.g. [Deason et al. 2022](#); [Tau et al. 2025](#); [Cooper et al. 2025](#)). The accreted stars are expected to be mostly centrally concentrated, with only a small fraction of them being observable as an extended stellar halo beyond the transition radius, defined as the radius where the ex-situ component dominates over the in-situ one ([Cooper et al. 2025](#); [Celiz et al. 2025](#)). In the [Cooper et al. \(2025\)](#) simulations, the transition radius for an IC 10-like galaxy occurs at values below 10 kpc, consistent with the radius of  $\sim 5$  kpc where our profile starts to deviate from the one-component Sérsic model. Assuming that the second, more extended component in our fit is entirely due to accreted stars, we would end up with an ex-situ fraction of  $\sim 13\text{--}26\%$ , (where the large range reflects the uncertainty in the background and foreground contamination to the star count profile), larger than what typically predicted by the simulations. On the other hand, [Tau et al. \(2025\)](#) argue that, for galaxies with the mass of IC 10, the outer stellar haloes are largely dominated by in-situ material formed in the inner regions of the galaxies and subsequently ejected into the outskirts during interactions and merger events with satellite galaxies. In this scenario, the stellar mass accreted by IC 10 could be lower than what inferred from the fit to the extended component.

## 6. Summary

- Through *Euclid* VIS and NISP photometry of resolved stars, we characterised the extended old (age  $\gtrsim 1\text{--}2$  Gyr) stellar component of IC 10 traced by RGB stars out to a SMA of about  $35'$  ( $\sim 8$  kpc), reaching an intrinsic (reddening-corrected) surface brightness limit of  $\mu_{H_E} \sim 29$  mag arcsec $^{-2}$ . While earlier studies predicted that the old stellar population of IC 10 could extend to very large distances, this work provides the first robust evidence that it does so, reaching such large radii and faint surface brightness levels.
- Thanks to the large sample of well-measured RGB stars, we infer a robust distance estimate through the RGB tip method. We obtain a distance modulus of  $(m - M)_0 = 24.41 \pm 0.05$ , corresponding to  $D = 762 \pm 20$  kpc, in good agreement with the recent measures by Sanna et al. (2008), McQuinn et al. (2017b), and Dell’Agli et al. (2018).
- The old stellar component shows a regular, mildly elliptical morphology ( $e = 0.12$ ) within SMA  $\sim 20'$  but, at larger radii, asymmetries emerge, particularly a stellar excess to the north-west that may indicate tidal interaction. Interestingly, this excess lies in the same direction as a previously identified  $\sim 17$  kpc-long H $\alpha$  structure interpreted as evidence of a past merger, raising the possibility, yet to be confirmed, that we are detecting a stellar counterpart to this feature. Another possibility is that the extended features that we see are due to the tidal interaction of IC 10 with M31.
- From RGB star counts, we derived the radial surface brightness profile of the old stellar component in IC 10. The main source of uncertainty is the correction for contamination from background galaxies and foreground stars, which becomes especially critical in the galaxy’s outskirts where the stellar density is low. This contamination is difficult to estimate reliably, as our CMD analysis reveals that RGB stars are still present at the edge of the *Euclid* field, indicating that we do not reach the full extent of the galaxy.
- Despite the uncertainty in the star counts at large galactocentric distances, the profile presents a clear excess in the outskirts compared to a single-component Sérsic model. In fact, the surface brightness profile of IC 10 is best described by a two-component model: an inner Sérsic profile (with  $n \sim 1.0\text{--}1.1$ ,  $r_e \sim 1$  kpc) and an outer component (that we tentatively fit with an exponential disc) that becomes dominant beyond  $\sim 5$  kpc, for which the fit parameters are more uncertain. This second, extended stellar component may trace the ex-situ material acquired during the past merging history of IC 10 with smaller satellites, or in-situ material stripped from its tidal interaction with M31.
- From the parameters of our profile fit, we estimate a stellar mass of  $M_\star = (6.7\text{--}8.1) \times 10^8 M_\odot$  in stars older than  $\sim 1$  Gyr, which is higher than previous estimates for IC 10. The extended stellar disc accounts for approximately 13–26% of the total mass in old stars, a higher fraction than typically predicted by cosmological simulations for the ex-situ component, although such simulations also allow for accreted fractions up to 100% in some cases.
- Our *Euclid* data provide unprecedented depth and spatial resolution over a wide field-of-view, far surpassing all previous studies of IC 10. They showcase the transformative impact of deep, wide-field, space-based imaging for studies of nearby galaxies, which will fully flourish in the coming years as subsequent *Euclid* data releases enable homogeneous analyses across large galaxy samples, and as the Roman Space Telescope begins scientific operations.

**Acknowledgements.** We thank N. Sanna for providing the HST photometric catalog of IC 10. FA acknowledge funding from the Italian INAF MINI GRANT RSN2:C33C24001360005 and project PRIN MUR 2022 (code 2022ARWP9C) “Early Formation and Evolution of Bulge and HalO (EFEBHO)”, PI: Marconi, M., funded by European Union–Next Generation EU. This research has made use of the NASA/IPAC Extragalactic Database (NED), which is funded by the National Aeronautics and Space Administration and operated by the California Institute of Technology. This research has made use of AutoProf, a package for galaxy image photometry (Stone et al. 2021), and on Astropy (<http://www.astropy.org>), a community-developed core Python package and an ecosystem of tools and resources for astronomy (Astropy Collaboration et al. 2013, 2018, 2022). This research has also made use of Photutils, an Astropy package for detection and photometry of astronomical sources (Bradley et al. 2023). This work has made use of the Early Release Observations (ERO) data from the Euclid mission of the European Space Agency (ESA), 2024, (<https://doi.org/10.57780/esa-qmocze3>). The Euclid Consortium acknowledges the European Space Agency and a number of agencies and institutes that have supported the development of *Euclid*, in particular the Agenzia Spaziale Italiana, the Austrian Forschungsförderungsgesellschaft funded through BMIMI, the Belgian Science Policy, the Canadian Euclid Consortium, the Deutsches Zentrum für Luft- und Raumfahrt, the DTU Space and the Niels Bohr Institute in Denmark, the French Centre National d’Etudes Spatiales, the Fundação para a Ciência e a Tecnologia, the Hungarian Academy of Sciences, the Ministerio de Ciencia, Innovación y Universidades, the National Aeronautics and Space Administration, the National Astronomical Observatory of Japan, the Nederlandse Onderzoekschool Voor Astronomie, the Norwegian Space Agency, the Research Council of Finland, the Romanian Space Agency, the Swiss Space Office (SSO) at the State Secretariat for Education, Research, and Innovation (SERI), and the United Kingdom Space Agency. A complete and detailed list is available on the *Euclid* web site ([www.euclid-ec.org/consortium/community/](http://www.euclid-ec.org/consortium/community/)).

## References

Annibali, F., Beccari, G., Bellazzini, M., et al. 2020, MNRAS, 491, 5101  
 Annibali, F., Nipoti, C., Ciotti, L., et al. 2016, ApJ, 826, L27  
 Ashley, T., Elmegreen, B. G., Johnson, M., et al. 2014, AJ, 148, 130  
 Astropy Collaboration, Price-Whelan, A. M., Lim, P. L., et al. 2022, ApJ, 935, 167  
 Astropy Collaboration, Price-Whelan, A. M., Sipőcz, B. M., et al. 2018, AJ, 156, 123  
 Astropy Collaboration, Robitaille, T. P., Tollerud, E. J., et al. 2013, A&A, 558, A33  
 Battaglia, G., Rejkuba, M., Tolstoy, E., Irwin, M. J., & Beccari, G. 2012, MNRAS, 424, 1113  
 Beccari, G., Bellazzini, M., Fraternali, F., et al. 2014, A&A, 570, A78  
 Bedin, L. R. 2025, A&A, 704, A193  
 Bekki, K. & Chiba, M. 2001, ApJ, 558, 666  
 Bellazzini, M. 2008, Mem. Soc. Astron. Italiana, 79, 440  
 Bellazzini, M., Beccari, G., Fraternali, F., et al. 2014, A&A, 566, A44  
 Bellazzini, M., Beccari, G., Oosterloo, T. A., et al. 2011, A&A, 527, A58  
 Bellazzini, M. & Pascale, R. 2024, A&A, 691, A42  
 Belokurov, V. & Koposov, S. E. 2016, MNRAS, 456, 602  
 Belokurov, V., Zucker, D. B., Evans, N. W., et al. 2006, ApJ, 642, L137  
 Bennet, P., Patel, E., Sohn, S. T., et al. 2024, ApJ, 971, 98  
 Bernard, E. J., Ferguson, A. M. N., Barker, M. K., et al. 2012, MNRAS, 426, 3490  
 Binder, B. A., Lazarus, R., Thoresen, M., Laycock, S., & Bhattacharya, S. 2025, ApJ, 991, 27  
 Bradley, L., Sipőcz, B., Robitaille, T., et al. 2023, astropy/photutils: 1.10.0  
 Bressan, A., Marigo, P., Girardi, L., et al. 2012, MNRAS, 427, 127  
 Brunthaler, A., Reid, M. J., Falcke, H., Henkel, C., & Menten, K. M. 2007, A&A, 462, 101  
 Bullock, J. S. & Johnston, K. V. 2005, ApJ, 635, 931  
 Caffau, E., Ludwig, H. G., Steffen, M., Freytag, B., & Bonifacio, P. 2011, Sol. Phys., 268, 255  
 Carlin, J. L., Garling, C. T., Peter, A. H. G., et al. 2019, ApJ, 886, 109  
 Celiz, B. M., Navarro, J. F., & Abadi, M. G. 2025, arXiv e-prints, arXiv:2510.18971  
 Chen, Y., Bressan, A., Girardi, L., et al. 2015, MNRAS, 452, 1068  
 Chen, Y., Girardi, L., Bressan, A., et al. 2014, MNRAS, 444, 2525  
 Chiti, A., Frebel, A., Simon, J. D., et al. 2021, Nature Astronomy, 5, 392  
 Collins, M. L. M., Read, J. I., Ibata, R. A., et al. 2021, MNRAS, 505, 5686  
 Cooper, A. P., Cole, S., Frenk, C. S., et al. 2010, MNRAS, 406, 744  
 Cooper, A. P., Frenk, C. S., Hellwing, W. A., & Bose, S. 2025, MNRAS, 540, 2049  
 Correnti, M., Annibali, F., Bellazzini, M., et al. 2025, ApJ, 982, 31  
 Crnojević, D., Sand, D. J., Spekkens, K., et al. 2016, ApJ, 823, 19

Crowther, P. A. & Bibby, J. L. 2009, A&A, 499, 455

Cuillandre, J.-C., Bertin, E., Bolzonella, M., et al. 2025, A&A, 697, A6

De Lucia, G. & Helmi, A. 2008, MNRAS, 391, 14

de Vaucouleurs, G., de Vaucouleurs, A., Corwin, Jr., H. G., et al. 1991, Third Reference Catalogue of Bright Galaxies (Springer, New York)

Deason, A. J., Bose, S., Fattah, A., et al. 2022, MNRAS, 511, 4044

Decleir, M., Gordon, K. D., Andrews, J. E., et al. 2022, ApJ, 930, 15

Dell'Agli, F., Di Criscienzo, M., Ventura, P., et al. 2018, MNRAS, 479, 5035

Demers, S., Battinelli, P., & Letarte, B. 2004, A&A, 424, 125

Diemand, J., Kuhlen, M., Madau, P., et al. 2008, Nature, 454, 735

Euclid Collaboration: Cropper, M., Al-Bahlawan, A., Amiaux, J., et al. 2025, A&A, 697, A2

Euclid Collaboration: Jahnke, K., Gillard, W., Schirmer, M., et al. 2025, A&A, 697, A3

Euclid Collaboration: Mellier, Y., Abdurro'uf, Acevedo Barroso, J., et al. 2025, A&A, 697, A1

Euclid Collaboration: Romelli, E., Kümmel, M., Dole, H., et al. 2025, A&A, in press (Euclid Q1 SI), <https://doi.org/10.1051/0004-6361/202554586>, arXiv:2503.15305

Euclid Collaboration: Scaramella, R., Amiaux, J., Mellier, Y., et al. 2022, A&A, 662, A112

Fakhouri, O., Ma, C.-P., & Boylan-Kolchin, M. 2010, MNRAS, 406, 2267

Ferguson, A. M. N., Irwin, M. J., Ibata, R. A., Lewis, G. F., & Tanvir, N. R. 2002, AJ, 124, 1452

Fitzpatrick, E. L., Massa, D., Gordon, K. D., Bohlin, R., & Clayton, G. C. 2019, ApJ, 886, 108

Gaia Collaboration, Montegriffo, P., Bellazzini, M., et al. 2023a, A&A, 674, A33

Gaia Collaboration, Prusti, T., de Bruijne, J. H. J., et al. 2016, A&A, 595, A1

Gaia Collaboration, Vallenari, A., Brown, A. G. A., et al. 2023b, A&A, 674, A1

Gerbrandt, S. A. N., McConnachie, A. W., & Irwin, M. 2015, MNRAS, 454, 1000

Gholami, M., Javadi, A., Mahani, H., et al. 2025, AJ, 170, 54

Girardi, L., Barbieri, M., Groenewegen, M. A. T., et al. 2012, in Astrophysics and Space Science Proceedings, Vol. 26, Red Giants as Probes of the Structure and Evolution of the Milky Way, 165

Girardi, L., Groenewegen, M. A. T., Hatziminaoglou, E., & da Costa, L. 2005, A&A, 436, 895

Golini, G., Montes, M., Carrasco, E. R., Román, J., & Trujillo, I. 2024, A&A, 684, A99

Gordon, K. D., Cartledge, S., & Clayton, G. C. 2009, ApJ, 705, 1320

Gordon, K. D., Clayton, G. C., Decleir, M., et al. 2023, ApJ, 950, 86

Gordon, K. D., Misselt, K. A., Bouwman, J., et al. 2021, ApJ, 916, 33

Higgs, C. R., McConnachie, A. W., Annau, N., et al. 2021, MNRAS, 503, 176

Howell, J. M., Ferguson, A. M. N., Larsen, S. S., et al. 2025, A&A, submitted, arXiv:2509.10440

Hoyt, T. J. 2023, Nature Astronomy, 7, 590

Huchtmeier, W. K. 1979, A&A, 75, 170

Hunt, L., Annibali, F., Cuillandre, J.-C., et al. 2025, A&A, 697, A9

Hunter, D. A. 2001, ApJ, 559, 225

Ibata, R., Irwin, M., Lewis, G., Ferguson, A. M. N., & Tanvir, N. 2001a, Nature, 412, 49

Ibata, R., Irwin, M., Lewis, G. F., & Stolte, A. 2001b, ApJ, 547, L133

Jacobs, B. A., Rizzi, L., Tully, R. B., et al. 2009, AJ, 138, 332

Jensen, J., Hayes, C. R., Sestito, F., et al. 2024, MNRAS, 527, 4209

Johnston, K. V., Bullock, J. S., Sharma, S., et al. 2008, ApJ, 689, 936

Johnston, K. V., Majewski, S. R., Siegel, M. H., Reid, I. N., & Kunkel, W. E. 1999, AJ, 118, 1719

Kado-Fong, E., Greene, J. E., Greco, J. P., et al. 2020, AJ, 159, 103

Kado-Fong, E., Sanderson, R. E., Greene, J. E., et al. 2022, ApJ, 931, 152

Kang, H. D. & Ricotti, M. 2019, MNRAS, 488, 2673

Kirby, E. M., Jerjen, H., Ryder, S. D., & Driver, S. P. 2008, AJ, 136, 1866

Kniazev, A. Y., Brosch, N., Hoffman, G. L., et al. 2009, MNRAS, 400, 2054

Koch, E. W., Leroy, A. K., Rosolowsky, E. W., et al. 2025, ApJS, 279, 35

Koposov, S. E., Walker, M. G., Belokurov, V., et al. 2018, MNRAS, 479, 5343

Kroupa, P. 2001, MNRAS, 322, 231

Kroupa, P. 2002, Science, 295, 82

Kroupa, P., Weidner, C., Pfamm-Altenburg, J., et al. 2013, in Planets, Stars and Stellar Systems. Volume 5: Galactic Structure and Stellar Populations, ed. T. D. Oswalt & G. Gilmore, Vol. 5, 115

Laureijs, R., Amiaux, J., Arduini, S., et al. 2011, ESA/SRE(2011)12, arXiv:1110.3193

Lee, A. J., Freedman, W. L., Madore, B. F., et al. 2025, ApJ, 985, 182

Lee, H., McCall, M. L., Kingsburgh, R. L., Ross, R., & Stevenson, C. C. 2003, AJ, 125, 146

Lee, M. G., Freedman, W. L., & Madore, B. F. 1993, ApJ, 417, 553

Liralalato, M., Bedin, L. R., Griggio, M., et al. 2024, A&A, 692, A96

Łokas, E. L., Gajda, G., & Kazantzidis, S. 2013, MNRAS, 433, 878

Madden, S. C., Rémy-Ruyer, A., Galametz, M., et al. 2013, PASP, 125, 600

Madore, B. F. & Freedman, W. L. 1995, AJ, 109, 1645

Madore, B. F. & Freedman, W. L. 2020, AJ, 160, 170

Magrini, L. & Gonçalves, D. R. 2009, MNRAS, 398, 280

Mancera Piña, P. E., Golini, G., Trujillo, I., & Montes, M. 2024, A&A, 689, A344

Marigo, P., Girardi, L., Bressan, A., et al. 2017, ApJ, 835, 77

Martin, G., Jackson, R. A., Kaviraj, S., et al. 2021, MNRAS, 500, 4937

Martin, G., Watkins, A. E., Dubois, Y., et al. 2025, MNRAS, 541, 1831

Martin, N. F., de Jong, J. T. A., & Rix, H.-W. 2008, ApJ, 684, 1075

Martínez-Delgado, D., Gabany, R. J., Crawford, K., et al. 2010, AJ, 140, 962

Martínez-Delgado, D., Peñarrubia, J., Gabany, R. J., et al. 2008, ApJ, 689, 184

Massari, D., Dalessandro, E., Erkal, D., et al. 2025, A&A, 697, A8

Massey, P. & Armandroff, T. E. 1995, AJ, 109, 2470

McConnachie, A. W. 2012, AJ, 144, 4

McConnachie, A. W., Higgs, C. R., Thomas, G. F., et al. 2021, MNRAS, 501, 2363

McMonigal, B., Bate, N. F., Lewis, G. F., et al. 2014, MNRAS, 444, 3139

McQuinn, K. B. W., Boyer, M. L., Mitchell, M. B., et al. 2017a, ApJ, 834, 78

McQuinn, K. B. W., Skillman, E. D., Dolphin, A. E., Berg, D., & Kennicutt, R. 2017b, AJ, 154, 51

Milone, A. P., Piotto, G., Bedin, L. R., et al. 2012, A&A, 540, A16

Moffat, A. F. J. 1969, A&A, 3, 455

Muñoz, R. R., Majewski, S. R., & Johnston, K. V. 2008, ApJ, 679, 346

Nally, C., Jones, O. C., Lenkić, L., et al. 2024, MNRAS, 531, 183

Namumba, B., Carignan, C., Foster, T., & Deg, N. 2019, MNRAS, 490, 3365

Nersesian, A., Xilouris, E. M., Bianchi, S., et al. 2019, A&A, 624, A80

Nidever, D. L., Ashley, T., Slater, C. T., et al. 2013, ApJ, 779, L15

Pace, A. B. 2024, arXiv e-prints, arXiv:2411.07424

Pastorelli, G., Marigo, P., Girardi, L., et al. 2020, MNRAS, 498, 3283

Pastorelli, G., Marigo, P., Girardi, L., et al. 2019, MNRAS, 485, 5666

Paudel, S., Smith, R., Yoon, S. J., Calderón-Castillo, P., & Duc, P.-A. 2018, ApJS, 237, 36

Peñarrubia, J., Navarro, J. F., McConnachie, A. W., & Martin, N. F. 2009, ApJ, 698, 222

Peebles, P. J. E. 1982, ApJ, 263, L1

Peng, E. W., Ferguson, H. C., Goudfrooij, P., et al. 2011, ApJ, 730, 23

Pillepich, A., Madau, P., & Mayer, L. 2015, ApJ, 799, 184

Pilyugin, L. S., Grebel, E. K., & Kniazev, A. Y. 2014, AJ, 147, 131

Poulain, M., Marleau, F. R., Habas, R., et al. 2021, MNRAS, 506, 5494

Richer, M. G., Bullejos, A., Borissova, J., et al. 2001, A&A, 370, 34

Román, J., Sánchez-Alarcón, P. M., Knapen, J. H., & Peletier, R. 2023, A&A, 671, L7

Ryś, A., Grocholski, A. J., van der Marel, R. P., Aloisi, A., & Annibali, F. 2011, A&A, 530, A23

Sacchi, E., Bellazzini, M., Annibali, F., et al. 2024, A&A, 691, A65

Salaris, M. & Cassisi, S. 1998, MNRAS, 298, 166

Sales, L. V., Wetzel, A., & Fattah, A. 2022, Nature Astronomy, 6, 897

Salomon, J.-B., Ibata, R., Reylé, C., et al. 2021, MNRAS, 507, 2592

Sanna, N., Bono, G., Stetson, P. B., et al. 2010, ApJ, 722, L244

Sanna, N., Bono, G., Stetson, P. B., et al. 2008, ApJ, 688, L69

Sarajedini, A., Bedin, L. R., Chaboyer, B., et al. 2007, AJ, 133, 1658

Schlafly, E. F. & Finkbeiner, D. P. 2011, ApJ, 737, 103

Schlegel, D. J., Finkbeiner, D. P., & Davis, M. 1998, ApJ, 500, 525

Serenelli, A., Weiss, A., Cassisi, S., Salaris, M., & Pietrinferni, A. 2017, A&A, 606, A33

Sestito, F., Zaremba, D., Venn, K. A., et al. 2023, MNRAS, 525, 2875

Shostak, G. S. & Skillman, E. D. 1989, A&A, 214, 33

Smercina, A., Dalcanton, J. J., Williams, B. F., et al. 2023, ApJ, 957, 3

Springel, V., Frenk, C. S., & White, S. D. M. 2006, Nature, 440, 1137

Stetson, P. B. 1987, PASP, 99, 191

Stone, C. J., Arora, N., Courteau, S., & Cuillandre, J.-C. 2021, MNRAS, 508, 1870

Tang, J., Bressan, A., Rosenfield, P., et al. 2014, MNRAS, 445, 4287

Tarumi, Y., Yoshida, N., & Frebel, A. 2021, ApJ, 914, L10

Tau, E. A., Monachesi, A., Gomez, F. A., et al. 2025, A&A, 699, A93

Tehrani, K., Crowther, P. A., & Archer, I. 2017, MNRAS, 472, 4618

Tikhonov, N. A. & Galazutdinova, O. A. 2009, Astronomy Letters, 35, 748

Weisz, D. R., Dolphin, A. E., Skillman, E. D., et al. 2014, ApJ, 789, 147

Wheeler, C., Oñorbe, J., Bullock, J. S., et al. 2015, MNRAS, 453, 1305

White, S. D. M. & Rees, M. J. 1978, MNRAS, 183, 341

Wilcots, E. M. & Miller, B. W. 1998, AJ, 116, 2363

Willmer, C. N. A. 2018, ApJS, 236, 47

Young, T., Jerjen, H., López-Sánchez, Á. R., & Koribalski, B. S. 2014, MNRAS, 444, 3052

Zhang, S., Mackey, D., & Da Costa, G. S. 2021, MNRAS, 508, 2098

## Authors and affiliations

F. Annibali<sup>★1</sup>, A. M. N. Ferguson<sup>2</sup>, P. M. Sanchez-Alarcon<sup>3,4</sup>, P. Dimauro<sup>5,6</sup>, L. K. Hunt<sup>7</sup>, R. Pascale<sup>1</sup>, M. Bellazzini<sup>1</sup>, A. Lançon<sup>8</sup>, P. Jablonka<sup>9</sup>, J. M. Howell<sup>2</sup>, K. Voggel<sup>8</sup>, J.-C. Cuillandre<sup>10</sup>, Abdurro'uf<sup>11</sup>, G. Battaglia<sup>12</sup>, L. R. BEDIN<sup>13</sup>, Michele Cantiello<sup>14</sup>, D. Carollo<sup>15</sup>, P.-A. Duo<sup>8</sup>, S. S. Larsen<sup>16</sup>, M. Libralato<sup>13</sup>, F. R. Marleau<sup>17</sup>, D. Massari<sup>1</sup>, T. Saifollahi<sup>8</sup>, C. Tortora<sup>18</sup>, M. Urbano<sup>8</sup>, M. Gatto<sup>18</sup>, I. McDonald<sup>19</sup>, M. Baes<sup>20</sup>, J. Román<sup>21</sup>, E. Dalessandro<sup>1</sup>, E. Iodice<sup>18</sup>, R. Ragusa<sup>18</sup>, S. Pearson<sup>22</sup>, S. Andreon<sup>23</sup>, N. Auricchio<sup>1</sup>, C. Baccigalupi<sup>24,15,25,26</sup>, M. Baldi<sup>27,1,28</sup>, A. Balestra<sup>13</sup>, S. Bardelli<sup>1</sup>, P. Battaglia<sup>1</sup>, A. Biviano<sup>15,24</sup>, E. Branchini<sup>29,30,23</sup>, M. Brescia<sup>31,18</sup>, S. Camera<sup>32,33,34</sup>, G. Cañas-Herrera<sup>2,35</sup>, V. Capobianco<sup>34</sup>, C. Carbone<sup>36</sup>, J. Carretero<sup>37,38</sup>, S. Casas<sup>39,40</sup>, M. Castellano<sup>6</sup>, G. Castignani<sup>1</sup>, S. Cavuoti<sup>18,41</sup>, A. Cimatti<sup>42</sup>, C. Colodro-Conde<sup>3</sup>, G. Congedo<sup>2</sup>, C. J. Conselice<sup>19</sup>, L. Conversi<sup>43,44</sup>, Y. Copin<sup>45</sup>, F. Courbin<sup>46,47,48</sup>, H. M. Courtois<sup>49</sup>, M. Cropper<sup>50</sup>, H. Degaudenzi<sup>51</sup>, G. De Lucia<sup>15</sup>, H. Dole<sup>52</sup>, F. Dubath<sup>51</sup>, C. A. J. Duncan<sup>2</sup>, X. Dupac<sup>44</sup>, S. Escoffier<sup>53</sup>, M. Farina<sup>54</sup>, R. Farinelli<sup>1</sup>, S. Ferriol<sup>45</sup>, F. Finelli<sup>1,55</sup>, M. Frailis<sup>15</sup>, E. Franceschi<sup>1</sup>, M. Fumana<sup>36</sup>, S. Galeotta<sup>15</sup>, K. George<sup>56</sup>, B. Gillis<sup>2</sup>, C. Giocoli<sup>1,28</sup>, J. Gracia-Carpio<sup>57</sup>, A. Grazian<sup>13</sup>, F. Grupp<sup>57,58</sup>, S. V. H. Haugan<sup>59</sup>, H. Hoekstra<sup>35</sup>, W. Holmes<sup>60</sup>, I. M. Hook<sup>61</sup>, F. Hormuth<sup>62</sup>, A. Hornstrup<sup>63,64</sup>, K. Jahnke<sup>65</sup>, M. Jhabvala<sup>66</sup>, E. Keihänen<sup>67</sup>, S. Kermiche<sup>53</sup>, A. Kiesling<sup>60</sup>, B. Kubik<sup>45</sup>, M. Kümmel<sup>58</sup>, M. Kunz<sup>68</sup>, H. Kurki-Suonio<sup>69,70</sup>, R. Laureijs<sup>71</sup>, A. M. C. Le Brun<sup>72</sup>, S. Ligori<sup>34</sup>, P. B. Lilje<sup>59</sup>, V. Lindholm<sup>69,70</sup>, I. Lloro<sup>73</sup>, G. Mainetti<sup>74</sup>, D. Maino<sup>75,36,76</sup>, E. Maiorano<sup>1</sup>, O. Mansutti<sup>15</sup>, S. Marcin<sup>77</sup>, O. Marggraf<sup>78</sup>, M. Martinelli<sup>6,79</sup>, N. Martinet<sup>80</sup>, F. Marulli<sup>81,1,28</sup>, R. J. Massey<sup>82</sup>, E. Medinaceli<sup>1</sup>, S. Mei<sup>83,84</sup>, M. Melchior<sup>85</sup>, Y. Mellier<sup>★86,87</sup>, M. Meneghetti<sup>1,28</sup>, E. Merlin<sup>6</sup>, G. Meylan<sup>9</sup>, A. Mora<sup>88</sup>, M. Moresco<sup>81,1</sup>, L. Moscardini<sup>81,1,28</sup>, R. Nakajima<sup>78</sup>, C. Neissner<sup>89,38</sup>, S.-M. Niemi<sup>90</sup>, C. Padilla<sup>89</sup>, S. Paltani<sup>51</sup>, F. Pasian<sup>15</sup>, K. Pedersen<sup>22</sup>, W. J. Percival<sup>91,92,93</sup>, V. Pettorino<sup>90</sup>, S. Pires<sup>10</sup>, G. Polenta<sup>94</sup>, M. Poncet<sup>95</sup>, L. A. Popa<sup>96</sup>, L. Pozzetti<sup>1</sup>, F. Raison<sup>57</sup>, R. Rebolo<sup>3,97,4</sup>, A. Renzi<sup>98,99</sup>, J. Rhodes<sup>60</sup>, G. Riccio<sup>18</sup>, E. Romelli<sup>15</sup>, M. Roncarelli<sup>1</sup>, R. Saglia<sup>58,57</sup>, Z. Saki<sup>100,101,102</sup>, D. Sapone<sup>103</sup>, B. Sartoris<sup>58,15</sup>, M. Schirmer<sup>65</sup>, P. Schneider<sup>78</sup>, A. Secroun<sup>53</sup>, G. Seidel<sup>65</sup>, S. Serrano<sup>104,105,106</sup>, P. Simon<sup>78</sup>, C. Sirignano<sup>98,99</sup>, G. Sirri<sup>28</sup>, L. Stanco<sup>99</sup>, J. Steinwagner<sup>57</sup>, P. Tallada-Crespi<sup>37,38</sup>, A. N. Taylor<sup>2</sup>, I. Tereno<sup>107,108</sup>, N. Tessore<sup>50</sup>, S. Toft<sup>109,110</sup>, R. Toledo-Moreo<sup>111</sup>, F. Torradefot<sup>38,37</sup>, I. Tutusaus<sup>106,104,101</sup>, L. Valenziano<sup>1,55</sup>, J. Valiviita<sup>69,70</sup>, T. Vassallo<sup>15</sup>, A. Veropalumbo<sup>23,30,29</sup>, Y. Wang<sup>112</sup>, J. Weller<sup>58,57</sup>, G. Zamorani<sup>1</sup>, I. A. Zinchenko<sup>113</sup>, E. Zucca<sup>1</sup>, J. García-Bellido<sup>114</sup>, J. Martín-Fleitas<sup>115</sup>, and V. Scottez<sup>86,116</sup>

<sup>1</sup> INAF-Osservatorio di Astrofisica e Scienza dello Spazio di Bologna, Via Piero Gobetti 93/3, 40129 Bologna, Italy

<sup>2</sup> Institute for Astronomy, University of Edinburgh, Royal Observatory, Blackford Hill, Edinburgh EH9 3HJ, UK

<sup>3</sup> Instituto de Astrofísica de Canarias, E-38205 La Laguna, Tenerife, Spain

<sup>4</sup> Universidad de La Laguna, Dpto. Astrofísica, E-38206 La Laguna, Tenerife, Spain

<sup>5</sup> Observatorio Nacional, Rua General Jose Cristiano, 77-Bairro Imperial de Sao Cristovao, Rio de Janeiro, 20921-400, Brazil

<sup>6</sup> INAF-Osservatorio Astronomico di Roma, Via Frascati 33, 00078 Monteporzio Catone, Italy

<sup>7</sup> INAF-Osservatorio Astrofisico di Arcetri, Largo E. Fermi 5, 50125, Firenze, Italy

<sup>8</sup> Université de Strasbourg, CNRS, Observatoire astronomique de Strasbourg, UMR 7550, 67000 Strasbourg, France

<sup>9</sup> Institute of Physics, Laboratory of Astrophysics, Ecole Polytechnique Fédérale de Lausanne (EPFL), Observatoire de Sauverny, 1290 Versoix, Switzerland

<sup>10</sup> Université Paris-Saclay, Université Paris Cité, CEA, CNRS, AIM, 91191, Gif-sur-Yvette, France

<sup>11</sup> Department of Astronomy, Indiana University, 727 East Third Street, Bloomington, IN 47405, USA

<sup>12</sup> Instituto de Astrofísica de Canarias, E-38205 La Laguna; Universidad de La Laguna, Dpto. Astrofísica, E-38206 La Laguna, Tenerife, Spain

<sup>13</sup> INAF-Osservatorio Astronomico di Padova, Via dell'Osservatorio 5, 35122 Padova, Italy

<sup>14</sup> INAF - Osservatorio Astronomico d'Abruzzo, Via Maggini, 64100, Teramo, Italy

<sup>15</sup> INAF-Osservatorio Astronomico di Trieste, Via G. B. Tiepolo 11, 34143 Trieste, Italy

<sup>16</sup> Department of Astrophysics/IMAPP, Radboud University, PO Box 9010, 6500 GL Nijmegen, The Netherlands

<sup>17</sup> Universität Innsbruck, Institut für Astro- und Teilchenphysik, Technikerstr. 25/8, 6020 Innsbruck, Austria

<sup>18</sup> INAF-Osservatorio Astronomico di Capodimonte, Via Moiariello 16, 80131 Napoli, Italy

<sup>19</sup> Jodrell Bank Centre for Astrophysics, Department of Physics and Astronomy, University of Manchester, Oxford Road, Manchester M13 9PL, UK

<sup>20</sup> Sterrenkundig Observatorium, Universiteit Gent, Krijgslaan 281 S9, 9000 Gent, Belgium

<sup>21</sup> Departamento de Física de la Tierra y Astrofísica, Universidad Complutense de Madrid, Plaza de las Ciencias 2, E-28040 Madrid, Spain

<sup>22</sup> DARK, Niels Bohr Institute, University of Copenhagen, Jagtvej 155, 2200 Copenhagen, Denmark

<sup>23</sup> INAF-Osservatorio Astronomico di Brera, Via Brera 28, 20122 Milano, Italy

<sup>24</sup> IFPU, Institute for Fundamental Physics of the Universe, via Beirut 2, 34151 Trieste, Italy

<sup>25</sup> INFN, Sezione di Trieste, Via Valerio 2, 34127 Trieste TS, Italy

<sup>26</sup> SISSA, International School for Advanced Studies, Via Bonomea 265, 34136 Trieste TS, Italy

<sup>27</sup> Dipartimento di Fisica e Astronomia, Università di Bologna, Via Gobetti 93/2, 40129 Bologna, Italy

<sup>28</sup> INFN-Sezione di Bologna, Viale Berti Pichat 6/2, 40127 Bologna, Italy

<sup>29</sup> Dipartimento di Fisica, Università di Genova, Via Dodecaneso 33, 16146, Genova, Italy

<sup>30</sup> INFN-Sezione di Genova, Via Dodecaneso 33, 16146, Genova, Italy

<sup>31</sup> Department of Physics "E. Pancini", University Federico II, Via Cinthia 6, 80126, Napoli, Italy

<sup>32</sup> Dipartimento di Fisica, Università degli Studi di Torino, Via P. Giuria 1, 10125 Torino, Italy  
<sup>33</sup> INFN-Sezione di Torino, Via P. Giuria 1, 10125 Torino, Italy  
<sup>34</sup> INAF-Osservatorio Astrofisico di Torino, Via Osservatorio 20, 10025 Pino Torinese (TO), Italy  
<sup>35</sup> Leiden Observatory, Leiden University, Einsteinweg 55, 2333 CC Leiden, The Netherlands  
<sup>36</sup> INAF-IASF Milano, Via Alfonso Corti 12, 20133 Milano, Italy  
<sup>37</sup> Centro de Investigaciones Energéticas, Medioambientales y Tecnológicas (CIEMAT), Avenida Complutense 40, 28040 Madrid, Spain  
<sup>38</sup> Port d'Informació Científica, Campus UAB, C. Albareda s/n, 08193 Bellaterra (Barcelona), Spain  
<sup>39</sup> Institute for Theoretical Particle Physics and Cosmology (TTK), RWTH Aachen University, 52056 Aachen, Germany  
<sup>40</sup> Deutsches Zentrum für Luft- und Raumfahrt e. V. (DLR), Linder Höhe, 51147 Köln, Germany  
<sup>41</sup> INFN section of Naples, Via Cinthia 6, 80126, Napoli, Italy  
<sup>42</sup> Dipartimento di Fisica e Astronomia "Augusto Righi" - Alma Mater Studiorum Università di Bologna, Viale Berti Pichat 6/2, 40127 Bologna, Italy  
<sup>43</sup> European Space Agency/ESRIN, Largo Galileo Galilei 1, 00044 Frascati, Roma, Italy  
<sup>44</sup> ESAC/ESA, Camino Bajo del Castillo, s/n, Urb. Villafranca del Castillo, 28692 Villanueva de la Cañada, Madrid, Spain  
<sup>45</sup> Université Claude Bernard Lyon 1, CNRS/IN2P3, IP2I Lyon, UMR 5822, Villeurbanne, F-69100, France  
<sup>46</sup> Institut de Ciències del Cosmos (ICCUB), Universitat de Barcelona (IEEC-UB), Martí i Franquès 1, 08028 Barcelona, Spain  
<sup>47</sup> Institució Catalana de Recerca i Estudis Avançats (ICREA), Passeig de Lluís Companys 23, 08010 Barcelona, Spain  
<sup>48</sup> Institut de Ciències de l'Espany (IEEC-CSIC), Campus UAB, Carrer de Can Magrans, s/n Cerdanyola del Vallés, 08193 Barcelona, Spain  
<sup>49</sup> UCB Lyon 1, CNRS/IN2P3, IUF, IP2I Lyon, 4 rue Enrico Fermi, 69622 Villeurbanne, France  
<sup>50</sup> Mullard Space Science Laboratory, University College London, Holmbury St Mary, Dorking, Surrey RH5 6NT, UK  
<sup>51</sup> Department of Astronomy, University of Geneva, ch. d'Ecogia 16, 1290 Versoix, Switzerland  
<sup>52</sup> Université Paris-Saclay, CNRS, Institut d'astrophysique spatiale, 91405, Orsay, France  
<sup>53</sup> Aix-Marseille Université, CNRS/IN2P3, CPPM, Marseille, France  
<sup>54</sup> INAF-Istituto di Astrofisica e Planetologia Spaziali, via del Fosso del Cavaliere, 100, 00100 Roma, Italy  
<sup>55</sup> INFN-Bologna, Via Irnerio 46, 40126 Bologna, Italy  
<sup>56</sup> University Observatory, LMU Faculty of Physics, Scheinerstr. 1, 81679 Munich, Germany  
<sup>57</sup> Max Planck Institute for Extraterrestrial Physics, Giessenbachstr. 1, 85748 Garching, Germany  
<sup>58</sup> Universitäts-Sternwarte München, Fakultät für Physik, Ludwig-Maximilians-Universität München, Scheinerstr. 1, 81679 München, Germany  
<sup>59</sup> Institute of Theoretical Astrophysics, University of Oslo, P.O. Box 1029 Blindern, 0315 Oslo, Norway  
<sup>60</sup> Jet Propulsion Laboratory, California Institute of Technology, 4800 Oak Grove Drive, Pasadena, CA, 91109, USA  
<sup>61</sup> Department of Physics, Lancaster University, Lancaster, LA1 4YB, UK  
<sup>62</sup> Felix Hormuth Engineering, Goethestr. 17, 69181 Leimen, Germany  
<sup>63</sup> Technical University of Denmark, Elektrovej 327, 2800 Kgs. Lyngby, Denmark  
<sup>64</sup> Cosmic Dawn Center (DAWN), Denmark  
<sup>65</sup> Max-Planck-Institut für Astronomie, Königstuhl 17, 69117 Heidelberg, Germany  
<sup>66</sup> NASA Goddard Space Flight Center, Greenbelt, MD 20771, USA  
<sup>67</sup> Department of Physics and Helsinki Institute of Physics, Gustaf Hällströmin katu 2, University of Helsinki, 00014 Helsinki, Finland  
<sup>68</sup> Université de Genève, Département de Physique Théorique and Centre for Astroparticle Physics, 24 quai Ernest-Ansermet, CH-1211 Genève 4, Switzerland  
<sup>69</sup> Department of Physics, P.O. Box 64, University of Helsinki, 00014 Helsinki, Finland  
<sup>70</sup> Helsinki Institute of Physics, Gustaf Hällströmin katu 2, University of Helsinki, 00014 Helsinki, Finland  
<sup>71</sup> Kapteyn Astronomical Institute, University of Groningen, PO Box 800, 9700 AV Groningen, The Netherlands  
<sup>72</sup> Laboratoire d'étude de l'Univers et des phénomènes eXtremes, Observatoire de Paris, Université PSL, Sorbonne Université, CNRS, 92190 Meudon, France  
<sup>73</sup> SKAO, Jodrell Bank, Lower Withington, Macclesfield SK11 9FT, UK  
<sup>74</sup> Centre de Calcul de l'IN2P3/CNRS, 21 avenue Pierre de Coubertin 69627 Villeurbanne Cedex, France  
<sup>75</sup> Dipartimento di Fisica "Aldo Pontremoli", Università degli Studi di Milano, Via Celoria 16, 20133 Milano, Italy  
<sup>76</sup> INFN-Sezione di Milano, Via Celoria 16, 20133 Milano, Italy  
<sup>77</sup> University of Applied Sciences and Arts of Northwestern Switzerland, School of Computer Science, 5210 Windisch, Switzerland  
<sup>78</sup> Universität Bonn, Argelander-Institut für Astronomie, Auf dem Hügel 71, 53121 Bonn, Germany  
<sup>79</sup> INFN-Sezione di Roma, Piazzale Aldo Moro, 2 - c/o Dipartimento di Fisica, Edificio G. Marconi, 00185 Roma, Italy  
<sup>80</sup> Aix-Marseille Université, CNRS, CNES, LAM, Marseille, France  
<sup>81</sup> Dipartimento di Fisica e Astronomia "Augusto Righi" - Alma Mater Studiorum Università di Bologna, via Piero Gobetti 93/2, 40129 Bologna, Italy  
<sup>82</sup> Department of Physics, Institute for Computational Cosmology, Durham University, South Road, Durham, DH1 3LE, UK  
<sup>83</sup> Université Paris Cité, CNRS, Astroparticule et Cosmologie, 75013 Paris, France  
<sup>84</sup> CNRS-UCB International Research Laboratory, Centre Pierre Binétruy, IRL2007, CPB-IN2P3, Berkeley, USA  
<sup>85</sup> University of Applied Sciences and Arts of Northwestern Switzerland, School of Engineering, 5210 Windisch, Switzerland  
<sup>86</sup> Institut d'Astrophysique de Paris, 98bis Boulevard Arago, 75014, Paris, France  
<sup>87</sup> Institut d'Astrophysique de Paris, UMR 7095, CNRS, and Sorbonne Université, 98 bis boulevard Arago, 75014 Paris, France  
<sup>88</sup> Telespazio UK S.L. for European Space Agency (ESA), Camino bajo del Castillo, s/n, Urbanizacion Villafranca del Castillo, Villanueva de la Cañada, 28692 Madrid, Spain  
<sup>89</sup> Institut de Física d'Altes Energies (IFAE), The Barcelona Institute of Science and Technology, Campus UAB, 08193 Bellaterra (Barcelona), Spain  
<sup>90</sup> European Space Agency/ESTEC, Keplerlaan 1, 2201 AZ Noordwijk, The Netherlands  
<sup>91</sup> Waterloo Centre for Astrophysics, University of Waterloo, Waterloo, Ontario N2L 3G1, Canada  
<sup>92</sup> Department of Physics and Astronomy, University of Waterloo, Waterloo, Ontario N2L 3G1, Canada  
<sup>93</sup> Perimeter Institute for Theoretical Physics, Waterloo, Ontario N2L 2Y5, Canada  
<sup>94</sup> Space Science Data Center, Italian Space Agency, via del Politecnico snc, 00133 Roma, Italy  
<sup>95</sup> Centre National d'Etudes Spatiales – Centre spatial de Toulouse, 18 avenue Edouard Belin, 31401 Toulouse Cedex 9, France

<sup>96</sup> Institute of Space Science, Str. Atomistilor, nr. 409 Măgurele, Ilfov, 077125, Romania  
<sup>97</sup> Consejo Superior de Investigaciones Científicas, Calle Serrano 117, 28006 Madrid, Spain  
<sup>98</sup> Dipartimento di Fisica e Astronomia "G. Galilei", Università di Padova, Via Marzolo 8, 35131 Padova, Italy  
<sup>99</sup> INFN-Padova, Via Marzolo 8, 35131 Padova, Italy  
<sup>100</sup> Institut für Theoretische Physik, University of Heidelberg, Philosophenweg 16, 69120 Heidelberg, Germany  
<sup>101</sup> Institut de Recherche en Astrophysique et Planétologie (IRAP), Université de Toulouse, CNRS, UPS, CNES, 14 Av. Edouard Belin, 31400 Toulouse, France  
<sup>102</sup> Université St Joseph; Faculty of Sciences, Beirut, Lebanon  
<sup>103</sup> Departamento de Física, FCFM, Universidad de Chile, Blanco Encalada 2008, Santiago, Chile  
<sup>104</sup> Institut d'Estudis Espacials de Catalunya (IEEC), Edifici RDIT, Campus UPC, 08860 Castelldefels, Barcelona, Spain  
<sup>105</sup> Satlantis, University Science Park, Sede Bld 48940, Leioa-Bilbao, Spain  
<sup>106</sup> Institute of Space Sciences (ICE, CSIC), Campus UAB, Carrer de Can Magrans, s/n, 08193 Barcelona, Spain  
<sup>107</sup> Departamento de Física, Faculdade de Ciências, Universidade de Lisboa, Edifício C8, Campo Grande, PT1749-016 Lisboa, Portugal  
<sup>108</sup> Instituto de Astrofísica e Ciências do Espaço, Faculdade de Ciências, Universidade de Lisboa, Tapada da Ajuda, 1349-018 Lisboa, Portugal  
<sup>109</sup> Cosmic Dawn Center (DAWN)  
<sup>110</sup> Niels Bohr Institute, University of Copenhagen, Jagtvej 128, 2200 Copenhagen, Denmark  
<sup>111</sup> Universidad Politécnica de Cartagena, Departamento de Electrónica y Tecnología de Computadoras, Plaza del Hospital 1, 30202 Cartagena, Spain  
<sup>112</sup> Caltech/IPAC, 1200 E. California Blvd., Pasadena, CA 91125, USA  
<sup>113</sup> Astronomisches Rechen-Institut, Zentrum für Astronomie der Universität Heidelberg, Mönchhofstr. 12-14, 69120 Heidelberg, Germany  
<sup>114</sup> Instituto de Física Teórica UAM-CSIC, Campus de Cantoblanco, 28049 Madrid, Spain  
<sup>115</sup> Aurora Technology for European Space Agency (ESA), Camino bajo del Castillo, s/n, Urbanizacion Villafranca del Castillo, Villanueva de la Cañada, 28692 Madrid, Spain  
<sup>116</sup> ICL, Junia, Université Catholique de Lille, LITL, 59000 Lille, France

---

\* e-mail: [francesca.annibali@inaf.it](mailto:francesca.annibali@inaf.it)  
\*\* Deceased

## Appendix A: Removal of MW contaminants from the IC 10 catalogue

In this section we describe in details the procedure adopted to remove MW contaminants (and residual background galaxies) from the IC 10 photometric catalogue.

The first step consists of cross-correlating the source catalogue with the *Gaia* data release 3 (DR3, [Gaia Collaboration et al. 2016, 2023b](#)) and looking for objects with a non-zero proper motion PM or with a parallax (Plx) larger than zero. For the match with the *Gaia* catalogue, we adopted a  $1''$  maximum tolerance in distance, but explored also lower matching radii finding the results to differ by just  $\sim 3\%$  for a tolerance radius as low as  $0''.1$ . Since IC 10 has a PM compatible with zero within the errors (e.g., [McConnachie et al. 2021; Bennet et al. 2024](#)), likely MW members were identified as those sources having a measured proper motion PM larger than  $3\sigma_{\text{PM}}$  or a parallax Plx larger than  $3\sigma_{\text{Plx}}$ , where  $\sigma_{\text{PM}}$  and  $\sigma_{\text{Plx}}$  are the *Gaia* errors on PM and Plx, respectively. With this approach, we effectively removed 7724 bright foreground stars with  $I_{\text{E},0} \lesssim 19$  (reddening corrected magnitudes) from our photometric catalogue. Second-epoch *Euclid* observations would be highly effective to remove most contaminants via proper motion membership ([Bedin 2025](#)).

The second step exploits a proper combination of VIS and NISP colours to remove Galactic M dwarf stars. The applied selection is illustrated in Fig. A.1, where we plot the reddening-corrected  $Y_{\text{E},0} - H_{\text{E},0}$  colour versus the  $I_{\text{E},0} - H_{\text{E},0}$  colour for the entire catalogue after removal of *Gaia* sources. At  $I_{\text{E},0} - H_{\text{E},0} \lesssim 1$ , giant and dwarf stars populate the same diagram locus, since their colours are degenerate for early spectral types; as a consequence, it is not possible to disentangle bluer dwarf stars from giant stars in IC 10 (mainly RGB and asymptotic giant branch stars). On the other hand, for  $I_{\text{E},0} - H_{\text{E},0} \gtrsim 1$ , the colours of dwarfs and giants start to diverge, with Galactic M dwarfs forming a  $Y_{\text{E},0} - H_{\text{E},0}$  relatively bluer sequence than giant stars in IC 10, as showcased in Fig. 10 of [H25](#) based on a comparison of the TRI-LEGAL Galactic model ([Girardi et al. 2005, 2012](#)) with stellar isochrones in the  $Y_{\text{E},0} - H_{\text{E},0}$  versus the  $I_{\text{E},0} - H_{\text{E},0}$  diagram. By removing sources at  $I_{\text{E},0} - H_{\text{E},0} \gtrsim 1$ ,  $Y_{\text{E},0} - H_{\text{E},0} \lesssim 0$ , as outlined in Fig. A.1, we eliminate the vast majority of Galactic M dwarf interlopers. The use of reddening-corrected magnitudes guarantees the cleanest possible separation between the giant and dwarf sequences.

The selection described above also allows the removal of residual compact red galaxies that survived the initial cuts based on photometry at different apertures, as illustrated in Fig. 2. These red galaxies form a separate sequence with  $Y_{\text{E},0} - H_{\text{E},0}$  colours intermediate between that defined by Galactic M dwarfs and that populated by asymptotic giant branch (AGB) stars in IC 10. A visual inspection of these objects in the VIS image shows in fact that they are associated with surrounding extended emission, with asymmetric or irregular morphology, confirming their extragalactic nature. This selection also removes spurious detections with  $Y_{\text{E},0} - H_{\text{E},0}$  colours redder than the AGB and the thermal pulsing AGB sequence, typically located at the edge of detectors, as illustrated in Fig. A.1.

Figure A.1 also shows a very blue sequence of objects, with  $I_{\text{E},0} - H_{\text{E},0} \lesssim -1$  and  $Y_{\text{E},0} - H_{\text{E},0} \lesssim -0.5$ . Based on their position in the colour-colour diagram and in the CMDs presented in Sect. 3, it is not possible to determine whether these sources are young luminous ‘blue plume’ (BP) stars in IC 10 or Galactic white dwarfs (WDs), and thus we retain them in our catalogue. Nonetheless, their quite uniform

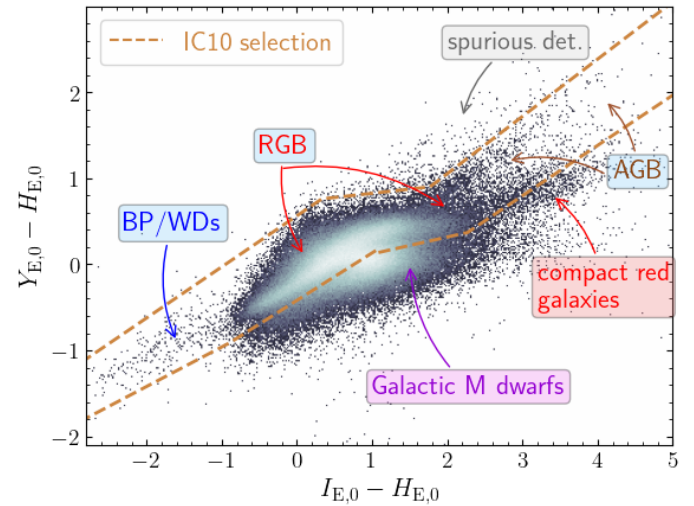


**Fig. A.1.**  $Y_{\text{E},0} - H_{\text{E},0}$  versus  $I_{\text{E},0} - H_{\text{E},0}$  diagram for sources in the IC 10 photometric catalogue, after removal of bright  $I_{\text{E},0} < 19$  MW stars in *Gaia* DR3 and after reddening correction from the map of Fig. 4b. The locations of Galactic M dwarf stars, RGB and AGB stars in IC 10, background compact red galaxies, and residual spurious detection are indicated. The bluest objects could be either young BP stars in IC 10 or Galactic WDs. The dashed orange polygon indicates our selection, aimed at retaining the largest possible number of stars belonging to IC 10 while removing Galactic M dwarf contaminants, compact red galaxies, and residual spurious detections (see text for details).

spatial distribution across the entire *Euclid* field, shown in Fig. A.2, suggests that they are mainly Galactic WDs, with a marginal contribution from young BP stars in IC 10. Despite the very well-known presence of recent star formation in IC 10 ([Massey & Armandroff 1995; Crowther & Bibby 2009; Tehrani et al. 2017; Gholami et al. 2025](#)), luminous blue stars are mainly concentrated in the innermost crowded regions and are affected by severe blending; thus they have likely been removed from our catalogue by selection criteria aimed at rejecting extended sources. In Fig. A.2 we also display the spatial distributions for the selected Galactic M dwarfs and compact red galaxies to show that they are distributed quite uniformly over the *Euclid* FoV as we would expect from foreground and background contaminants.

## Appendix B: Additional Colour-Magnitude Diagrams

In this section we present, for completeness, the  $I_{\text{E},0}$  versus  $I_{\text{E},0} - Y_{\text{E},0}$  (panel a) and  $I_{\text{E},0}$  versus  $I_{\text{E},0} - H_{\text{E},0}$  CMDs (panel b) of the stars in IC 10. As in Fig. 5, the CMDs were corrected for spatially variable reddening as described in Sect. 2.2, and cleaned for background galaxies and foreground stars as detailed in Sect. 2.3. The displayed CMDs contain a total of 213 882 sources. The black dashed curves denote the 50% completeness levels averaged over the entire *Euclid* FoV. The curves were obtained from the results of the artificial star tests presented in Sect. C and were corrected adopting a median reddening value of  $E(B - V) = 0.8$  for proper comparison with the displayed CMDs.

## Appendix C: Artificial star tests and completeness

To evaluate the completeness of our photometry at different magnitudes, we perform artificial star tests; such an analysis also

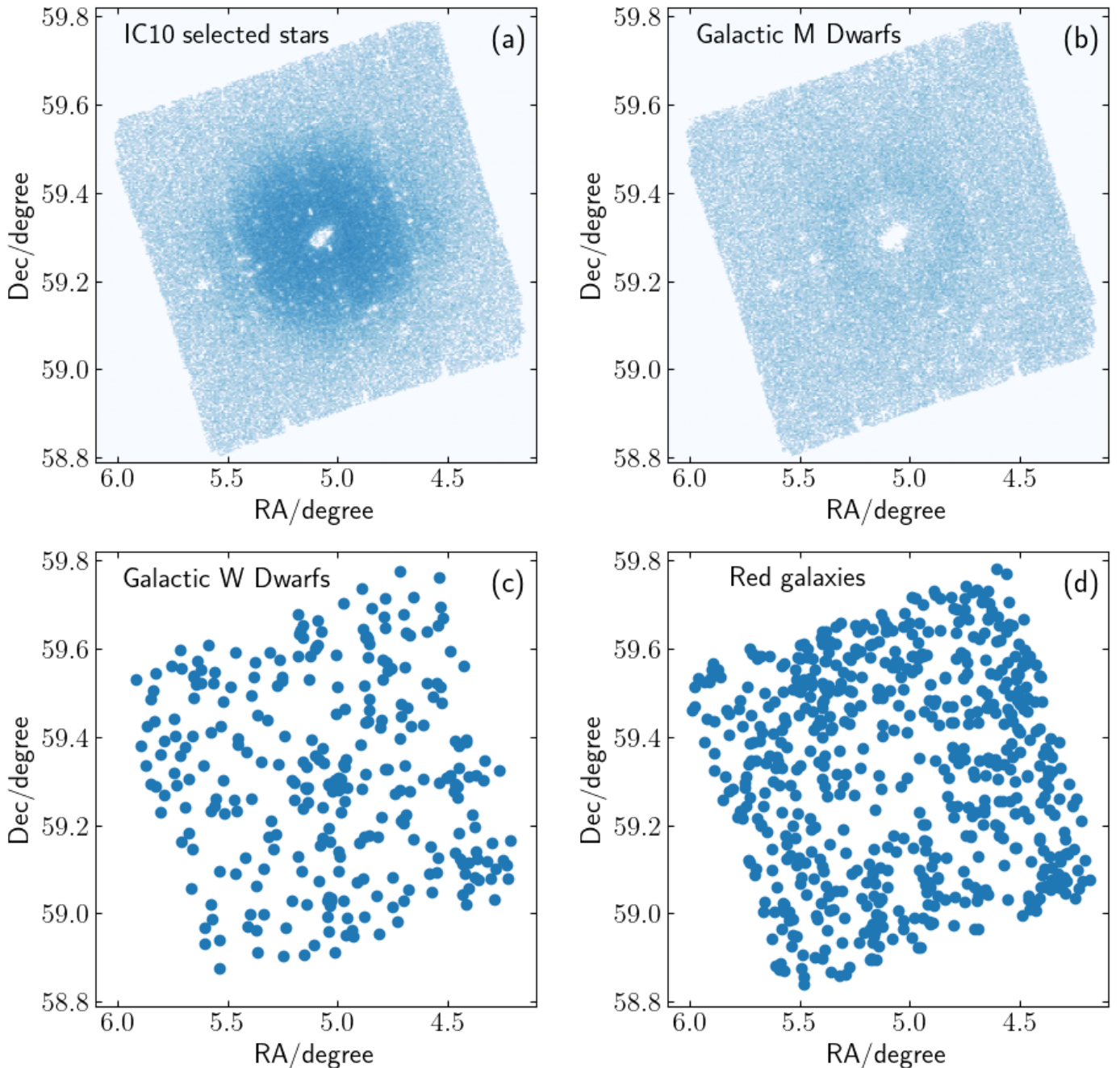


**Fig. A.2.** Spatial distribution of stars in IC 10 after removal of different contaminants (panel *a*) versus Galactic M dwarfs (panel *b*), Galactic white dwarfs (panel *c*) and compact red galaxies (panel *d*).

quantifies the observational effects associated with the data reduction process, such as the accuracy of the photometric measurements and the probability of blending in crowded regions. The tests were performed by adding artificial stars to the  $I_E$ ,  $Y_E$ ,  $J_E$ , and  $H_E$  images, and then reducing the frames following exactly the same procedure as for the real data.

To place artificial stars into the images, we first created PSF models for each of the 4 *Euclid* bands selecting the most isolated, bright, and unsaturated stars within the frames, and then running the PSF routine in DAOPHOT. To speed up the computation and better control the PSF, we divided each image into  $3 \times 3$  smaller subsections, and modelled for each band the nine PSFs with an analytic Moffat function (Moffat 1969) plus additive corrections derived from the residuals of the fit to the bright selected stars.

The additive corrections include only first-order derivatives of the PSF with respect to the  $X$  and  $Y$  positions in the sub-image, which is a reasonable choice given the smooth behaviour of the PSF over the *Euclid* FoV (C25).

To assign proper colours and magnitudes to the artificial stars, we exploited the deeper CMD of NGC 6822 (containing about 200 000 stars), the nearest dwarf irregular (at a distance of  $\sim 0.5$  Mpc) observed in the context of the Showcase Galaxies ERO (H25). The CMD of NGC 6822 was scaled to IC 10's distance and reddening, providing a sample of stars with colours compatible with those observed in IC 10 but extending to fainter magnitudes, as needed to properly evaluate the incompleteness at the faintest limits. Artificial stars with  $I_E$ ,  $Y_E$ ,  $J_E$ , and  $H_E$  magnitudes were extracted from this CMD and placed homogeneously

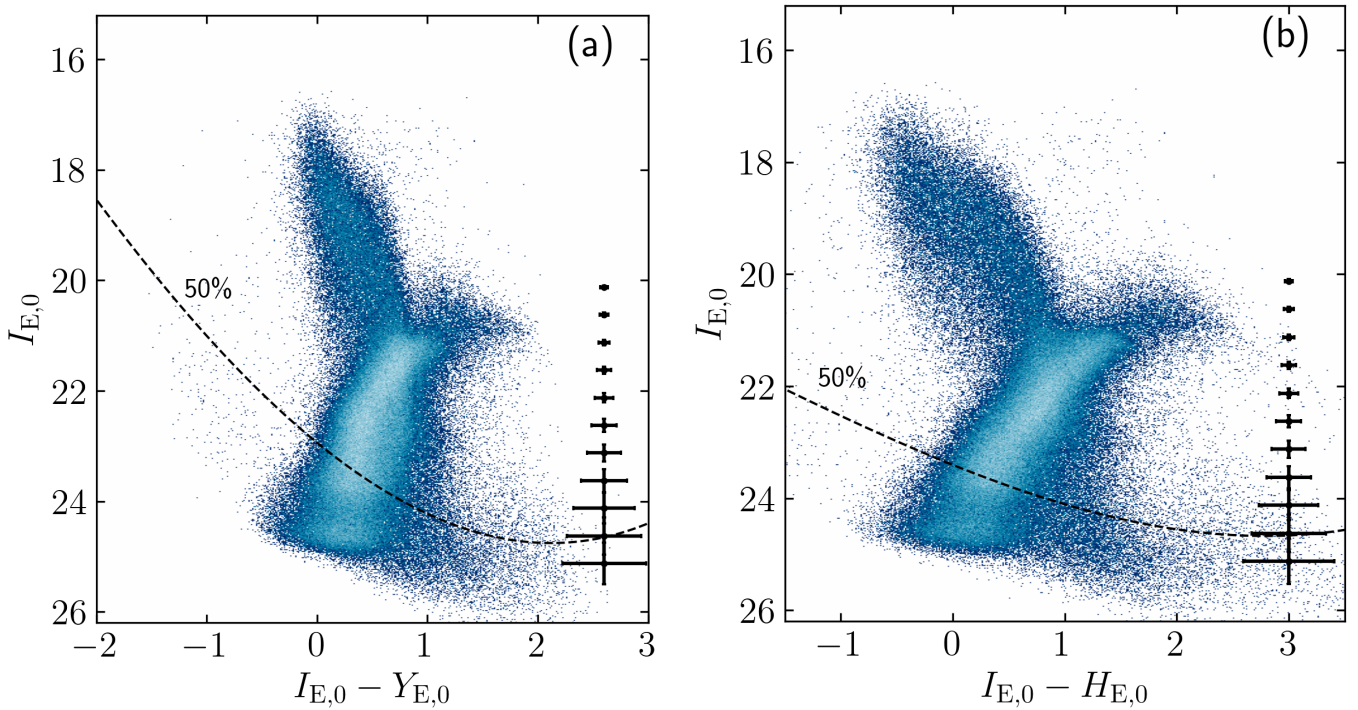


**Fig. B.1.**  $I_{E,0}$  versus  $I_{E,0} - Y_{E,0}$  (panel a) and  $I_{E,0}$  versus  $I_{E,0} - H_{E,0}$  (panel b) reddening-corrected CMDs after removal of foreground contaminants, as described in Sect. 2. The black dashed curves denote the average 50% completeness levels, corrected for the median reddening in IC 10.

on the images. In order to avoid artificial stars interfering with one another, thus creating spurious crowding, we added only 20 000 stars at a time for each of the nine image subsections and repeated the process 10 times (20 times for the innermost, crowded section), for a total of 2 million artificial stars simulated in each band. Each star was placed in the IC 10 image at the same exact position in both the VIS and NISP frames to properly evaluate our ability of recovering stars also as a function of their colours.

Then, the photometric reduction of the VIS and NISP frames containing both real and artificial stars, the match of the catalogues in the four  $I_E$ ,  $Y_E$ ,  $J_E$ , and  $H_E$  bands, and the selections of sources based on the DAOPHOT parameters were performed exactly as for the original images. In the end, the final catalogue with photometry in all four bands was cross-matched with the list of injected artificial stars. Once the 10 runs (or 20 for the innermost region) were completed for each of the nine image subsections, the outputs were joined together into a final master catalogue totalling 2 million simulated artificial stars.

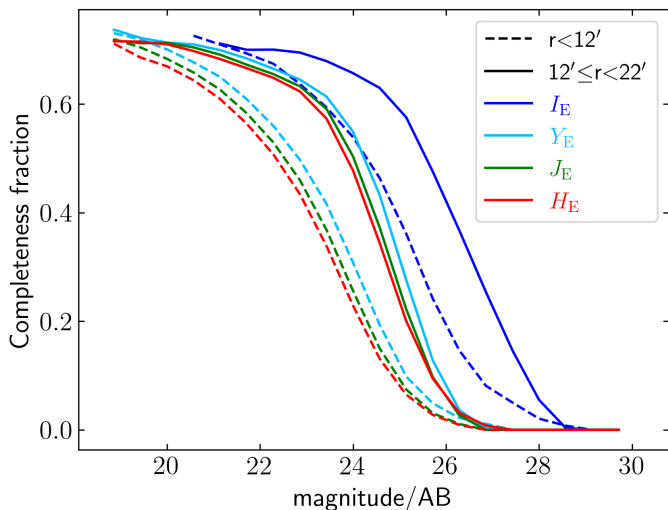
For each magnitude bin, the completeness was computed as the ratio of the number of remaining artificial stars over the number of added ones. The difference between the output and input magnitudes for the recovered stars provides a realistic measurement of the photometric uncertainties, with the exception of uncertainties related to the exact shape of the PSF.

The results of our artificial star experiments are illustrated in Figs. C.1, C.2, and C.3. Figure C.1 shows the completeness fraction as a function of (reddening-uncorrected) magnitude for different bands. We display the completeness both for an inner region at galactocentric distance of  $r \lesssim 12'$  and for an outer annulus at  $12' \lesssim r \lesssim 22'$ . As expected, completeness is lower in the centre than in the external region due to increased crowding: we infer 50% completeness at  $I_E \sim 24.3$  in the inner region while the same level is reached at  $I_E \sim 25.5$  in the external region. These values are similar to the completeness values obtained by

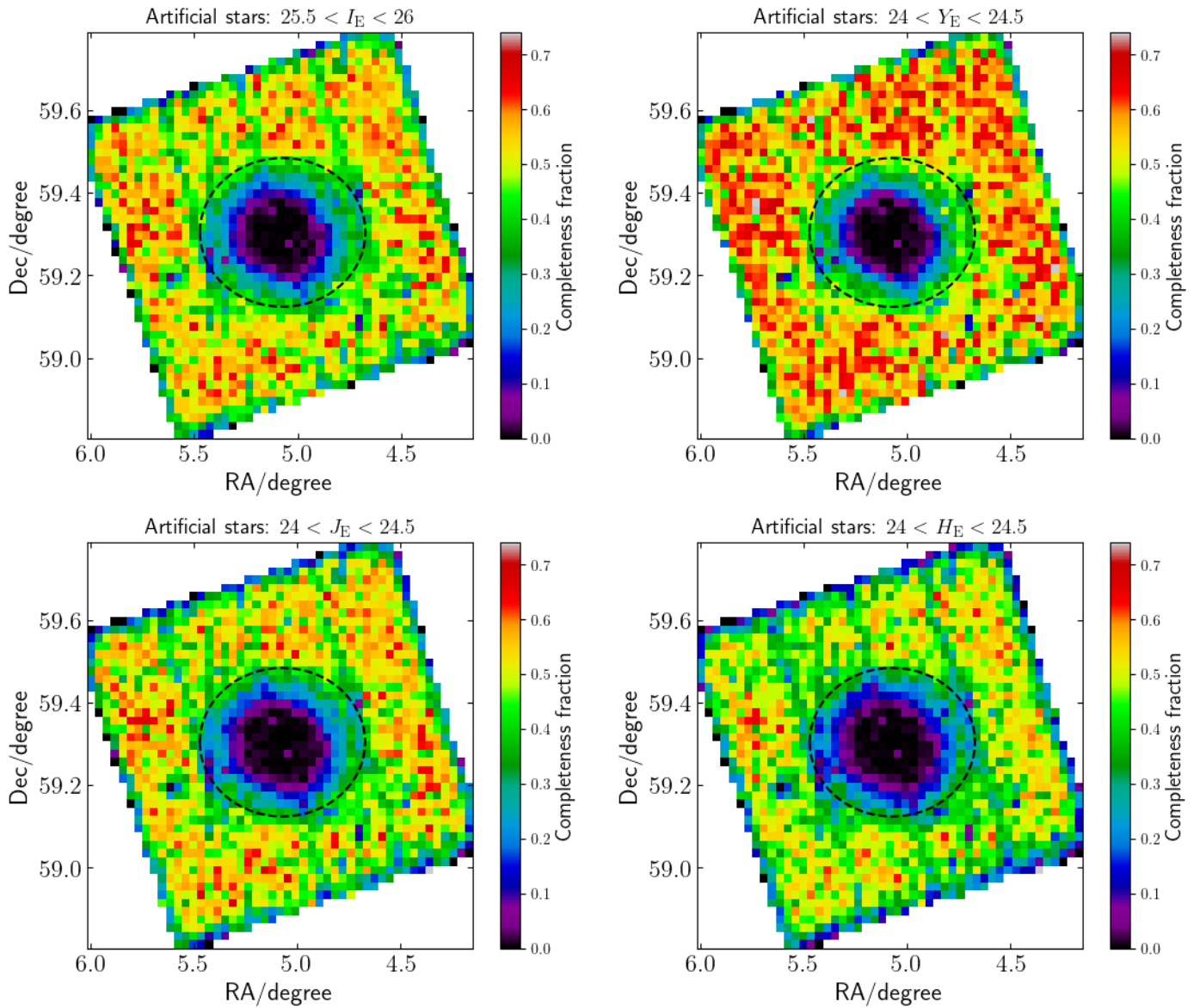
Massari et al. (2025) for the *Euclid* ERO data of NGC 6254, a Milky Way globular cluster. A maximum completeness below 80% is a consequence of stars having to spatially match in all four *Euclid* bands to appear in the final photometric catalogue, coupled with the presence of severe Galactic foreground star contamination. Artificial stars injected on top of bright saturated foreground stars tend to be lost due to the compromised photometry, explaining why even at the brightest magnitudes we never reach 100% completeness.

Figure C.2 illustrates the spatial variation of the completeness across the entire *Euclid* field of view. These maps were constructed for specific magnitude intervals tailored to each band: 25.5–26 mag for the  $I_E$  band, and 24–24.5 mag for the  $Y_E$ ,  $J_E$ , and  $H_E$  bands. The maps reveal a clear spatial trend, with completeness significantly decreasing toward the central crowded regions of IC 10. Conversely, in the outer, less crowded regions, the completeness remains relatively high, enabling a more reliable analysis of the faint, extended stellar populations of the galaxy.

Figure C.3 shows the distribution of the difference between output and input magnitudes as a function of the input magnitude for the recovered artificial stars across the different bands. In all bands, the distributions are not symmetric around zero, but become more and more skewed toward negative values at the faintest magnitudes, as also denoted by the behaviour of the median line. This trend is due to the increasing importance of blending at fainter magnitudes, which causes the flux of stars to be overestimated. The artificial star tests also indicate that the photometric accuracy is better in  $I_E$  than in  $Y_E$ ,  $J_E$ , and  $H_E$ , with  $\sigma_{I_E} \sim 0.1$  at 26 mag compared to  $\sigma_{NISP} \sim 0.2$  at 24 mag in the NISP bands. This effect is likely due to the undersampling of the *Euclid* PSF, which is worse for the NISP bands than for VIS (Euclid Collaboration: Mellier et al. 2025; Libralato et al. 2024).



**Fig. C.1.** Completeness fraction derived from artificial star tests as a function of magnitude in the four *Euclid* bands:  $I_E$  (blue),  $Y_E$  (cyan),  $J_E$  (green), and  $H_E$  (red). The dashed lines denote the completeness for a circular region within  $12'$  from the centre, while the solid lines are for an annulus at  $12' \leq r < 22'$ . The magnitudes shown here are not corrected for reddening.



**Fig. C.2.** Spatial distribution of completeness in different *Euclid* bands, as derived from artificial star experiments. The maps show the fraction of injected artificial stars that were successfully recovered by the photometric reduction process, after applying all selection criteria. Completeness is computed over the magnitude ranges 25.5–26 for the  $I_E$  band and 24–24.5 for the  $Y_E$ ,  $J_E$ , and  $H_E$  bands. The same black dashed ellipse as in Fig. 7 is overplotted for direct comparison with the RGB star density map. Note that no reddening correction was applied to the artificial star magnitudes prior to producing these maps.

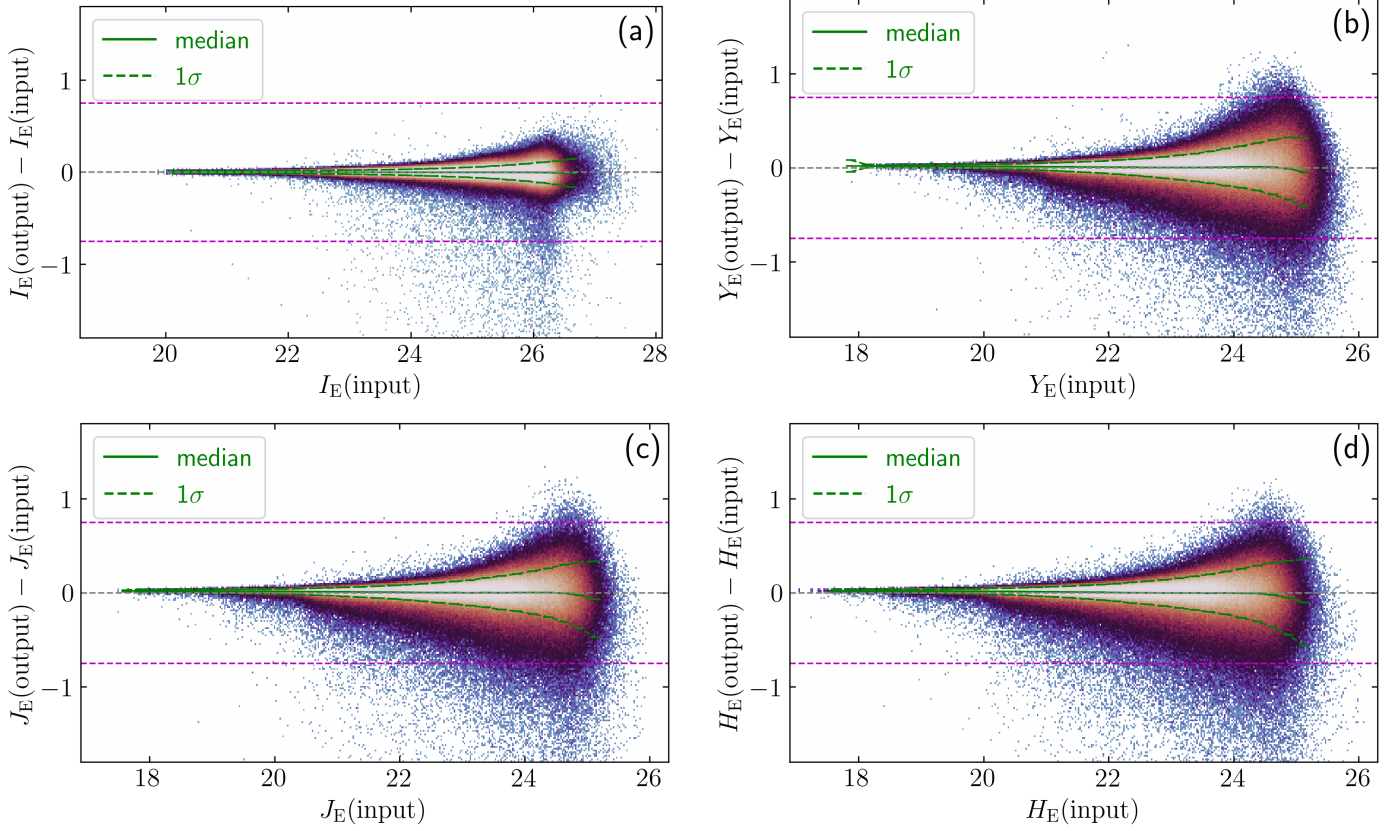


**Fig. C.3.** Distribution of the output minus input magnitudes ( $\Delta m$ ) for the artificial stars in different bands:  $I_E$  (panel a),  $Y_E$  (panel b),  $J_E$  (panel c), and  $H_E$  (panel d). The green continuous line and the dashed lines denote the median and the  $\pm 1\sigma$  regions of the distributions, respectively, while the magenta dashed horizontal lines correspond to values of  $\Delta m \pm 0.75$ . In all bands, the distributions appear asymmetric, with a larger number of stars exhibiting negative  $\Delta m$  values due to blending with neighbouring sources. For example, a star blended with another of equal flux will appear brighter by  $\Delta m = -0.75$ .